https://doi.org/10.5194/egusphere-2026-2734
Preprint. Discussion started: 11 June 2026

Determining optimal model height to represent mountain observations in atmospheric transport and inversion studies

Lilja Dahl[1,2], Martin Vojta[4], Ignacio Pisso[3], Rona L. Thompson[3], and Alessandro Bigi[1]

[1]Department of Engineering "Enzo Ferrari", University of Modena and Reggio Emilia (UniMoRe)
[2]University School for Advanced Studies in Pavia (IUSS Pavia), Pavia, Italy
[3]The Climate and Environmental Research Institute (NILU), Kjeller, Norway
[4]Department of Meteorology and Geophysics, University of Vienna, Vienna, Austria

Correspondence: Lilja Dahl (lilja.dahl@iusspavia.it)

Abstract. Accurate modelling atmospheric transport over complex terrain is challenging due to processes interacting with the orography and the use of finite resolution wind fields in Atmospheric Transport Models (ATMs). An unresolved issue is the representation of mountain stations within ATMs, and particularly the choice of model height that best represents mountain observations. This study proposes a methodology to determine optimal heights for representing mountain sites in ATMs, using FLEXPART driven by ECMWF ERA5 wind fields at two spatial resolutions. Three different release height methods were evaluated: i) sampling inlet height (S-rh), ii) an intermediate height based on model orography (P-rh), and iii) a varying release height determined by matching ERA5 potential temperature with observations (T-rh). A sensitivity analysis is presented, determining the optimal particle release height for three mountain sites and its influence on the simulated mixing ratios, using SF_6 as a tracer and two prior fluxes across different seasons and diurnal cycles. Results show that the model performance strongly depends on the release height choice, spatial resolution of the wind fields, station characteristics and atmospheric condition. The varying T-rh, generally provided a good representation of the observations across seasons and sites, although summer advection was not well captured. S-rh systematically underestimated observed variability, leading to a weaker source-receptor relationship (SRR) and biased posterior emissions. These findings highlight the importance of representing mountain stations in ATMs to reduce the model-data mismatch and that an inappropriate release height can lead to systematic bias of posterior flux estimates.

1 Introduction

The role of anthropogenic activity in increasing atmospheric abundance of greenhouse gases (GHGs) has been known to be important for decades, with carbon dioxide (CO_2) and methane (CH_4) having the highest positive mean effective radiative forcing (ERF), estimated to be 2.156 ± 0.259 W m^{-2} and 0.544 ± 0.109 W m^{-2}, relative to the period 1750-2019 (Forster et al., 2023). Ever since the Paris Agreement was adopted in 2015 to limit the global mean surface air temperature $\leq$2.0°C above preindustrial levels over a 20-year period (UNFCCC, 2015), a strong demand for independent methods to verify reported national GHG emission inventories (NGHGI) from Annex I countries emerged. One such prominent tool that can estimate GHG surface fluxes spatio-temporally is atmospheric inverse modeling, which combines measurements of atmospheric species

https://doi.org/10.5194/egusphere-2026-2734
Preprint. Discussion started: 11 June 2026

and atmospheric transport model (ATM) outputs with background mixing ratios to optimize a prior emission estimate. It is recommended as an independent observation-based verification method by the scientific community (Meijer et al., 2019) and the Intergovernmental Panel on Climate Change (IPCC et al., 2019). Up to today, this observation-based approach has been applied to estimate GHG surface fluxes on a global (Vojta et al., 2024), continental (including the Horizon European research projects: Paris https://horizoneurope-paris.eu/, Avengers https://avengers-project.eu/, and Eye-Clima https://eyeclima.eu/) (Bergamaschi et al., 2022; Vojta et al., 2025), national domains (Deng et al., 2022), and also for cities (Lian et al., 2023; Ponomarev et al., 2026). A major focus has been on comparing atmospheric inversion-based estimates at national scale with bottom-up NGHGI reported annually to the United Nations Framework Convention on Climate Change (UNFCCC). Atmospheric inverse modeling has also been successfully applied to independently verify NGHGI in Switzerland (Henne et al., 2016; Rust et al., 2022), in the UK (Manning et al., 2022; Munassar et al., 2023), and in Germany (Bruch et al., 2025), to name a few.

Atmospheric inversion emission estimates are associated with a number of uncertainties, in particular those pertaining to model representation, which include the uncertainty of modeled transport by the ATM and the finite resolution of the model and the emissions estimates. These uncertainties influence the agreement of the modeled mixing ratios with the observations (model data mismatch, MDM), and if they are not properly taken into account, can lead to errors in flux estimates obtained from atmospheric inversions. The ATM, either Eulerian (Hourdin and Armengaud, 1999) or Lagrangian Particle Dispersion Models (LPDM) e.g. the FLEXible PARTicle (FLEXPART) (Pisso et al., 2019) and Stochastic Time-Inverted Lagrangian Transport (STILT) (Lin et al., 2003) are commonly used to simulate atmospheric pollutants dispersion in the atmosphere at various temporal and spatial resolutions. A LPDM comparison study by Munassar et al. (2023), found that most errors are introduced by mesoscale ATM as representation errors when trying to resolve atmospheric transport at a finer spatial resolution, which is necessary to represent GHGs mole fractions high-frequency patterns in emissions (in this study for CO_2). Two inversion systems were compared using identical inversion set-ups (e.g. prior fluxes, boundary condition, and optimization method), but two different LPDMs, FLEXPART and STILT, and results showed that 61 % of the total discrepancies between the posterior CO_2 flux estimates were attributed to the use of various atmospheric transport schemes in the LPDMs (Munassar et al., 2023).

Notwithstanding their long residence time, long-lived GHG can exhibit strong spatial and vertical gradients with high mixing ratios in highly populated and industrialized valleys or basins, e.g. the Po valley in northern Italy, the Rhone valley in France, and the Ruhr valley in Germany, as they have a high density of emissions (Folini et al., 2008). A high mixing ratio can also be related to reduced atmospheric dispersion, e.g. due to ground-based inversion episodes, in particular, during wintertime, causing stagnation close to the surface (Giovannini et al., 2020). Observations for GHG are sparse, therefore, mountain stations are often used when they are available (e.g. those within the Global Atmospheric Watch (GAW) network), despite the complex orography, posing challenges for the simulation of the atmospheric processes. Challenges arise in accurately representing the upslope/downslope winds at mountain sites in ATMs and at finite resolution, i.e. the model orography does not match the actual height of the mountain. This is particularly the case when ATM is driven by coarse resolution meteorological wind fields, e.g. the ECMWF ERA5 reanalysis product (Hersbach et al., 2020) with a spatial resolution of $0.5° \times 0.5°$ (widely used

https://doi.org/10.5194/egusphere-2026-2734
Preprint. Discussion started: 11 June 2026

in atmospheric inversion studies), that lack a detailed representation of the orography at the mountain sites and the ATM might not have a suitable turbulence parameterization scheme to explain turbulence over complex terrain.

Several studies address uncertainties related to the ATM at mountain sites, and Folini et al. (2008), highlighted that particle release height in LPDM had a significant impact on simulated CO mixing ratios and that selecting a receptor height closer to the ground increased the average CO mixing ratios by nearly 50 %, while a higher release height led to a shorter residence time. Since potential temperature is a conserved quantity following the terrain, e.g. if air flows over a hill or mountain range the value of potential temperature is conserved, it lends itself as a possible quantity for selecting an appropriate model level for representing the mountain site, or for LPDMs, for particle release height. In addition, the potential temperature can be calculated from meteorological variables that are often measured alongside GHG measurements, as well as from meteorological fields. We propose a methodology to evaluate and select the optimal model height to represent mountain stations in ATM using potential temperature, to improve the model representation for mountain sites, and reduce errors associated with using these in atmospheric inversions. Our method uses the comparison of the model and observed potential temperature, and is evaluated at three mountain sites: Jungfraujoch (JFJ), Zugspitze (ZSF), and Schauinsland (SSL). They are situated in the European Alpine region, where air pollution and GHG emissions from nearby valleys can be transported with upward winds reaching the Alps (Diémoz et al., 2019) and occasionally to high mountain sites, depending on the atmospheric boundary layer (ABL) height. We applied FLEXPART to build the source-receptor matrix at the mountain sites and the Bayesian atmospheric inverse modeling framework FlexInvert (Thompson and Stohl, 2014) to better understand the impact of particle release height on top-down GHG flux estimates. Sulfur hexafluoride (SF_6) was used as a tracer, which is a potent GHG reported in NGHGI and, importantly, observations are available from several GAW mountain sites, which is not the case for other potential tracers such as Radon. Its atmospheric lifetime is estimated to be 850 years $(580 - 1400)$ (Ray et al., 2017) without significant tropospheric sinks, making it highly stable in the atmosphere and considered a suitable tracer for ATM validation and testing.

This study is organized as follows: A comprehensive description of the methodology is presented (Sect. 2), including input data and the setup of LPDM FLEXPART and atmospheric inversion, as well as the methodology for determining the optimal representation height for mountain sites in the ATM (Sect. 2.2.2). The results of simulated SF_6 mixing ratios at three mountain sites applying various release height scenarios in LPDM are presented in Sect. 3.1 and the impact of the model height selection on the optimized SF_6 emissions is given in Sect. 3.2.

2 Methodology

2.1 Source Receptor Relationship

Lagrangian Particle Dispersion Models (LPDMs) simulate trajectories of virtual particles represented as infinitesimally small air parcels that can be used to simulate atmospheric compounds (e.g., an aerosol particle, a specific gas species, or air) moving in the ambient flow. The transport is driven by advection i.e. the mean flow along with stoichastic turbulent and diffusive transport by subgrid processes such as turbulence, the gravitational settling, and other first-order loss processes e.g., radioactive decay or wet deposition (Thomson, 1987; Stohl et al., 2005).

https://doi.org/10.5194/egusphere-2026-2734
Preprint. Discussion started: 11 June 2026

A main advantage in the use of LPDMs for atmospheric transport is that it is not run on a grid with a prescribed resolution (as is the case with Eulerian models), but it has potentially an infinite resolution at the point from which particles are released. Therefore, it is suitable to investigate problems with different characteristic spatial scales, including regional inversion studies. Virtual particles can be released in two ways: 1) from a point or volume source and traced forward in time to model changes in atmospheric concentration or mixing ratio or 2) from receptor sites, e.g. measurement sites, and traced backward in time to determine the origin of the air masses and to so-called Source Receptor Relationships (SRRs), which describe the influence of fluxes (at a given spatiotemporal resolution) on an observation (Seibert and Frank, 2004). The relationship between the state vector $\mathbf{x}$ and the observed mole fraction $\mathbf{y}$ is described by the forward model, $\mathrm{H}(\mathbf{x})$, which is the modeled mole fraction of a given flux of $\mathbf{x}$ (Eq. 1). In this study, the source-receptor matrix operator, H, is the contribution of the emission sensitivity, $\mathrm{H}^{\mathrm{nest}}$ in the nested domain (see Sect.2.2) during the backward simulation time period and the background emission sensitivities, H^{bkg} that occur outside the nested domain, and contribution of the mole fractions to the observation prior to the simulation period, $\mathbf{y}^{ini}$. The state vector $\mathbf{x}$ is the combination of nested fluxes $\mathbf{x}^{nest}$ and background fluxes $\mathbf{x}^{bkg}$. A disadvantage of using LPDM is that the particles are traced backwards only for a limited time due to computational costs. Therefore, the initial mixing ratios $\mathbf{y}^{ini}$ must be accounted for at the point where the backtrajectories terminate (Thompson and Stohl, 2014). We apply daily global SF_6 mole fraction fields at $3^\circ \times 2^\circ$ spatial resolution from Vojta et al. (2022) to account for the initial condition.

$$\mathbf{y} = \mathrm{H}^{nest}\mathbf{x}^{nest} + \mathrm{H}^{bkg}\mathbf{x}^{bkg} + \mathbf{y}^{ini} = \mathrm{H}(\mathbf{x}) \tag{1}$$

2.2 Model domain

In this study, we apply the LPDM FLEXPART v10.4 (Pisso et al., 2019), driven by the ECMWF ERA5 hourly reanalysis product in GRIB2 format at two different horizontal resolutions, $0.5^\circ \times 0.5^\circ$ and $0.2^\circ \times 0.2^\circ$ and 137 terrain-following hybrid $\eta-$levels, to simulate the atmospheric transport of SF_6. From each receptor site (listed in Table 2), $10,000$ particles are released every hour (release heights are introduced in Sect. 2.2.2 and Table 3), and the trajectories are traced backwards in time for 7 days (see Table 1 for model setup and Figure 1 for the model domain) to obtain a 2D Source Receptor Relationship (SRR) field of the lowest layer, i.e. 0-100 m above ground level (agl). Two model domains are defined, a global domain and a nested domain that covers northern Italy and the Alps (4°E–16°E, 42°–50°N) with an output resolution of $1^\circ \times 1^\circ$ and $0.1^\circ \times 0.1^\circ$ respectively and 36 vertical levels agl.

To obtain a realistic SRR using FLEXPART, it must fulfill fundamental physical criteria of maintaining a well-mixed particle distribution, a proper coupling between wind shear and vertical turbulence, and adequate/high temporal resolution to resolve turbulent processes (Thomson, 1987; Lin et al., 2003). FLEXPART must therefore ensure that the initial 10,000 particles are well mixed throughout the 7-day simulation window. Otherwise, particles might either accumulate or dilute unrealistically. A configuration in FLEXPART that influences the turbulent velocity is LSYNCTIME and in this study, a short synchronization time step (LSYNCTIME = 600 s) was used to ensure frequent coupling between advection and turbulent processes, which is particularly important to maintain a well-mixed particle distribution under rapidly changing flow conditions in complex mountainous terrain. The high temporal resolution ensures that the particle velocities respond correctly to turbulent fluctuations

https://doi.org/10.5194/egusphere-2026-2734
Preprint. Discussion started: 11 June 2026

on timescales shorter than the Lagrangian time scale. Furthermore, a sub-grid scale parameterization scheme was applied to better resolve terrain features and thereby improve the representation of vertical mixing at mountain sites. The convective ABL scheme governs the interactions between wind shear and vertical turbulence and we used a Gaussian boundary layer scheme (CBLFLAG = 0) to ensure consistent vertical redistribution of particles. However, a more recent turbulence scheme was introduced in FLEXPART v10.4, accounting for the vertical skewness of updrafts and downdrafts, as well as the vertical gradients of air density (Pisso et al., 2019), which is especially important for accurately simulating atmospheric transport and dispersion from mountain sites. All these choices directly affect the velocity fluctuations that the virtual particles will experience (the FLEXPART configuration is given in the Appendix, Table A1).

During the simulation period, SF_6 is considered chemically inert, and no chemical decay processes were included in FLEXPART.

Table 1. Model domain and spatial resolution.

	Global	**Nested**
Domain	180°W–180°E 90°S–90°N	4°–16°E, 42°–50°N
Model output	$1° \times 1°$	$0.1° \times 0.1°$
ECMWF ERA5	$0.5° \times 0.5°$	$0.5° \times 0.5°$ / $0.2° \times 0.2°$

2.2.1 Mountain receptor sites

Atmospheric observations of SF_6 (reported as dry air mole fractions) and of meteorological variables such as temperature, pressure, and relative humidity was collected for the year 2019 from the three mountain sites which contribute to multiple internationally-coordinated monitoring networks e.g. the Advanced Global Atmospheric Gases Experiment (AGAGE), the Integrated Carbon Observation System (ICOS-RI), and/or the WMO/GAW. In Table 2, the altitude is the station sampling inlet and mountain elevation obtained from ICOS (https://data.icos-cp.eu/portal/) and WDCGG data portal (https://gaw.kishou.go.jp/), and the orography elevation is from the ERA5 wind fields at two different horizontal resolution.

Zugspitze (ZSF, 47°42'N, 10°98'E, 2670 m asl) and Schauinsland (SSL, 47°90'N, 7°92E, 1205 m asl) include hourly continuous SF_6 measurements using a Gas Chromotography-Electron Capture Detector (GC-ECD) analysis with a precision of 0.1 ppt. At Jungfraujoch (JFJ, 46°55'N, 7°99'E, 3585 m asl) SF_6 observations are collected every two hours using Gas Chromatography-Mass Spectrometry (GC-MS) with a "Medusa" sample processing system having a precision of 0.6 % (Simmonds et al., 2020). All three stations use the NOAA 2014 calibration scale. Nonetheless, SF_6 mixing ratios from the SSL station were significantly lower than the simulated background levels at JFJ and ZSF, exhibiting a fairly steady offset of ca. 0.55 ppt. Since an offset does not affect the goal of the study and the reliability of its results, this same offset was added to the SSL observations, along with a higher uncertainty for the atmospheric inversion.

https://doi.org/10.5194/egusphere-2026-2734
Preprint. Discussion started: 11 June 2026

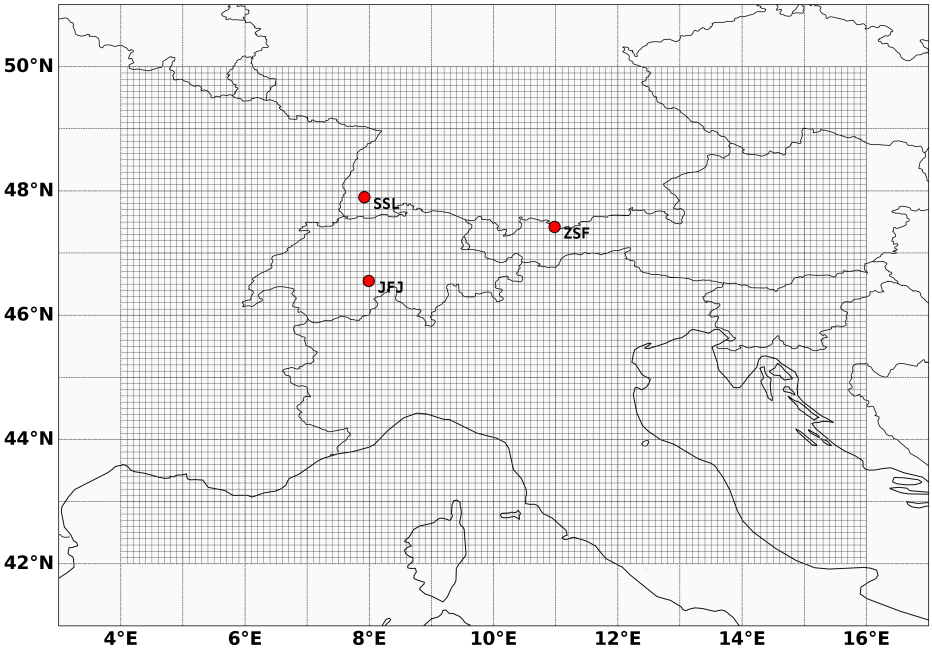

Figure 1. Nested domain with a grid resolution of 0.1°× 0.1° and 1°× 1° elsewhere. The three Alpine stations: JFJ, ZSF, and SSL are indicated with a red dot.

The two high Alpine sites JFJ and ZSF are compared with the lower mountain site SSL for the seasons JF (January and February), MAM (March, April, and May), JJA (June, July, and Aug) and SON (September, October, and November). December month was excluded due to missing wind fields at 0.2°×0.2° spatial resolution. We examined their mixing layer height (MLH) from FLEXPART, a proxy of the PBL (the minimum MLH is set to 100 m agl), to understand when the release height was above or below the MLH.

Table 2. Receptor sites.

Stations	**Name**	**lon**	**lat**	**Altitude** [m asl]	**ERA5** $\mathbf{0.5^\circ \times 0.5^\circ}$ **orog** [m asl]	**ERA5** $\mathbf{0.2^\circ \times 0.2^\circ}$ **orog** [m asl]
Jungfraujoch	JFJ	7.99	46.55	3585.0	2246.3	2121.3
Zugspitze	ZSF	10.98	47.42	2670.0	2101.8	1805.6
Schauinsland	SSL	7.92	47.90	1205.0	505.3	547.9

https://doi.org/10.5194/egusphere-2026-2734
Preprint. Discussion started: 11 June 2026

2.2.2 Determining optimal representation height

The optimal height to represent a mountain station in a model (for Lagrangian models this is the particle release height) was determined by matching the potential temperature (θ), computed from ERA5 meteorological variables (θ_{ERA5}), with the observed potential temperature (θ_{OBS}) at the measurement stations (STN). In FLEXPART, three release height scenarios were evaluated and compared: **1)** Virtual particles were released from a fixed point release height equal to the sampling station inlet elevation relative to sea level, and referred to as the sampling release height (S-rh). **2)** A fixed point release between the station sampling inlet elevation and the orography elevation in the ERA5 wind fields, referred to as the proxy release height (P-rh). **3)** An hourly point release with varying heights, calculated by matching $\theta_{\text{ERA5,STN}}$ with $\theta_{\text{OBS,STN}}$, and the release heights were estimated using the hypsometric equation (Eq. 3). This will be referred to as theta release height (T-rh).

The $\theta_{\text{OBS,STN}}$ was calculated using the observed temperature (T) and pressure (p) in Eq. 2 and θ can be defined as the temperature that an adiabatic air parcel would have if it moved adiabatically from pressure p_t to surface pressure p_s, corresponding to the geopotential height of Z_s and Z_t. It will be constant under adiabatic processes and is derived from the first law of thermodynamics and the ideal gas law for dry air. At mountain sites, θ increases monotonically with height and can therefore be used as a vertical coordinate.

$$\theta = T \cdot \left(\frac{p_s}{p_t}\right)^{\kappa} \tag{2}$$

Where κ is the Poisson constant ($\kappa = \mathrm{R}_d/c_p = 0.2854$), R_d being the specific gas constant for dry air ($R_d = \frac{R}{M_{\text{air}}} = \frac{8.314\,\mathrm{J\,K^{-1}\,mol^{-1}}}{28.97\,\mathrm{g\,mol^{-1}}} = 287\,\mathrm{J\,kg^{-1}\,K^{-1}}$). In the literature, the surface pressure p_s is commonly referred to as the reference sea level pressure $p_0 = 1013.25$ hPa, but in this study, p_s corresponds to the surface model pressure at the lowest $\eta-$level. The $\theta_{\text{ERA5,STN}}$ was calculated from the ERA5 fields, for 137 $\eta-$ levels, and for each time step. To identify which $\eta-$ level minimizes the difference between $\theta_{\text{ERA5,STN}}$ and $\theta_{\text{OBS,STN}}$, a linear fit of the vertical $\theta_{\text{ERA5,STN}}$ profile against pressure ($p_{\text{ERA5, STN}}$), for each time step, was matched with $\theta_{\text{OBS,STN}}$. However, the $p_{\text{ERA5, STN}}$ values for certain stations fluctuated beyond acceptable limits, resulting in excessively high release heights, and therefore, a criterion was defined by setting an upper and lower pressure limits. The highest pressure limit was set to be the pressure at the surface $\eta-$level, while the lowest pressure limit was defined as the $\mathrm{p}_{\text{ERA5, STN}}$ value closest to the observed pressure + 4 $\eta-$levels. The linear interpolation resulted in a smoother sub-grid estimate of $\theta_{\text{ERA5,STN}}$ values and was very close to $\theta_{\text{OBS,STN}}$, while selecting only the minimum absolute difference between $\theta_{\text{ERA5,STN}}$ and $\theta_{\text{OBS,STN}}$ produced some discontinuities and ignored the vertical gradient of $\theta_{\text{ERA5,STN}}$. The two different approaches are compared with the observed θ and illustrated in the Appendix A1− A4. The $\eta-$level where $\theta_{\text{ERA5,STN}}$ best matches $\theta_{\text{OBS,STN}}$ for each time step, was used to select the matching pressure level, and was then converted to geopotential height using the hypsometric equation expressed in Eq. 3, explaining the relationship between layer thickness and temperature (considering a constant temperature of the layer). A rolling mean of 8 hours was applied to $\mathrm{p}_{\text{ERA5, STN}}$ before calculating the release height to produce a smooth time series and avoid flat values during this capping procedure. The computed varying release heights (reported as monthly median values) for Jan, Apr, July and Oct 2019 are given in Table 3.

https://doi.org/10.5194/egusphere-2026-2734
Preprint. Discussion started: 11 June 2026

$$Z_{agl} = \frac{R_d}{g} \cdot \overline{T_v} \cdot \ln\left(\frac{p_s}{p_t}\right) \tag{3}$$

The hypsometric equation considers the humidity in the atmosphere from the virtual temperature $\overline{T_v} = \mathrm{T}(1+0.608 q_v)$, where the specific humidity q_v is the ratio of the mass of water vapor to the total mass of air ($m_{\mathrm{air}} = m_{\mathrm{dry\,air}} + m_{\mathrm{water\,vapor}}$). We did test this method by matching the equivalent potential temperature (θe), which considers moist air and estimated the height using $\overline{T_v}$ instead of θ in Eq. 3. Both the empirical Bucks/WMO formula (WMO, 2008) (using observed dew-point temperature (T_d) at JFJ, ZSF, and SSL site) and the Clausius-Clapeyron equation were tested to determine the saturation vapor pressure, and the latter was found to be the most suitable, as it is also used in FLEXPART. However, after analysing the vertical profiles of θe and θ at the three mountain sites JFJ, ZSF, and SSL, we found that the vertical profiles of θ were more monotonic than θe, making θ a more robust approach for selecting the release height.

https://doi.org/10.5194/egusphere-2026-2734
Preprint. Discussion started: 11 June 2026

Table 3. The various release heights applied in FLEXPART simulations for the three mountain sites for Jan, Apr, July, and Oct 2019.

Stations	ERA5 $0.5^\circ \times 0.5^\circ$			ERA5 $0.2^\circ \times 0.2^\circ$		
	T-rh median [Q_{25}, Q_{75}] [m agl]	**P-rh** [m agl]	**S-rh** [m agl]	**T-rh median** [Q_{25}, Q_{75}] [m agl]	**P-rh** [m agl]	**S-rh** [m agl]
JFJ	**Jan** 940.2 [719 , 1119.5]	669.4	1338.7	**Jan** 1199.1 [951.3 , 1402.3]	731.9	1463.7
	Apr 974.7 [743.4 , 1159.9]			**Apr** 1269.6 [1054.1, 1486.9]		
	July 736.3 [542.3 , 1040.1]			**July** 1134.8 [851.9 , 1347.2]		
	Oct 913.2 [699.4 , 1105.3]			**Oct** 1199.1 [951.3 , 1402.3]		
ZSF	**Jan** 197.8 [110.0 , 302.1]	284.1	568.20	**Jan** 51.0 [22.8 , 108.2]	432.2	864.36
	Apr 286.6 [158.5 , 415.3]			**Apr** 102.9[33.3 , 243.2]		
	July 215.3[70.6 , 336.4]			**July** 108.3 [24.4 , 260.9]		
	Oct 250.1 [146.6 , 359.9]			**Oct** 95.6 [38.6 , 180.2]		
SSL	**Jan** 660.1[516.2 , 817.0]	349.9	699.8	**Jan** 734.9 [598.3 , 879.0]	328.6	657.2
	Apr 601.5 [439.7 , 764.6]			**Apr** 626.3 [420.5 , 763.0]		
	July 609.5 [424.7 , 753.1]			**July** 616.0 [462.3 , 795.9]		
	Oct 565.2 [464.5 , 700.5]			**Oct** 648.5 [515.1 , 767.6]		

https://doi.org/10.5194/egusphere-2026-2734
Preprint. Discussion started: 11 June 2026

2.3 Model orography

A contour plot of the ERA5 orography of the three mountain sites is illustrated in Fig. 2a at 0.5°×0.5° and Fig. 2b at 0.2°×0.2° spatial resolution. The orography height from ERA5 at the mountain sites was derived from the nearest horizontal grid points, after allocating stations' actual coordinates to cell indices indicated as (i, j), but this introduced a systematic bias towards lower indices, i.e. the coordinates of the nearest grid points were shifted west and south of the actual location of the stations. A noticeable difference in altitude was observed when comparing the actual surface height at JFJ and ZSF sites with the surface height of the ERA5 orography at grid point (i, j) at two different spatial resolutions (Table 1). Fig. 2a highlighted that the grid point $(i+1, j)$, i.e., the grid point shifted horizontally to the east, results in coordinates closer in proximity to the actual geographical location of JFJ and the orography height of grid point (i, j) (Fig. 3a), shows a significantly lower orography height (1654.86 m) than the grid point $(i+1, j)$ (2246.27 m), horizontally shifted towards the east (Fig. 3b). Considering that JFJ is located on a mountain peak, the grid point $(i+1, j)$ represented the most suitable grid point for calculating $\theta_{\mathrm{ERA5,JFJ}}$ and obtain T-rh at 0.5°×0.5° horizontal resolution.

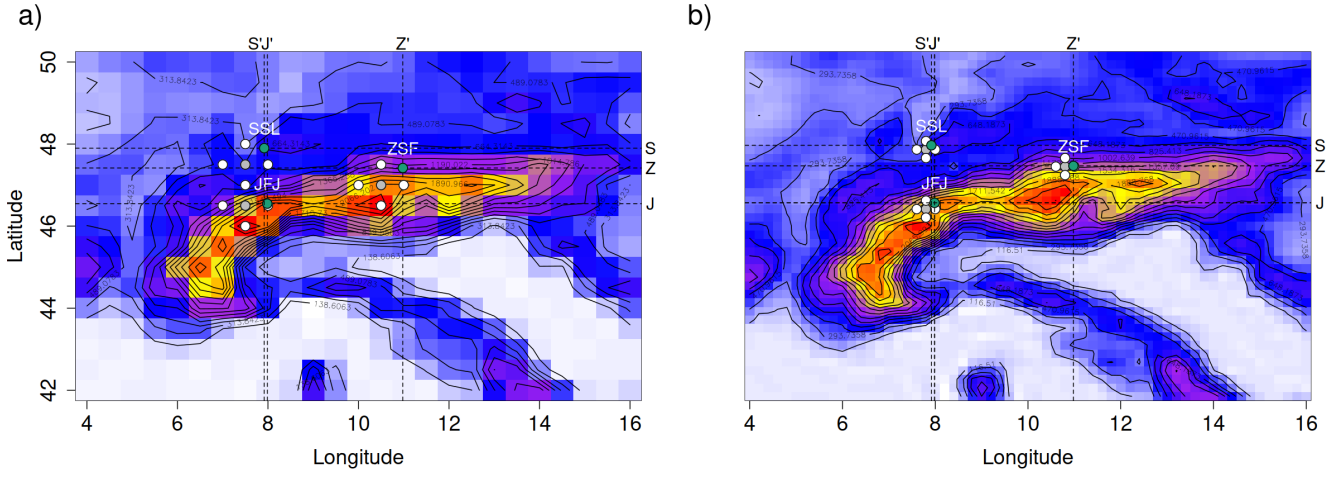

Figure 2. Contour plot a) at 0.5°×0.5° and b) 0.2°×0.2° spatial resolution. Red dots indicate the ERA5 central grid point (i,j) closest to the station's geographical location, white dots indicate the horizontal neighboring grid points adjacent to grid point (i,j) in grey, and green dots indicate the station's actual geographical location.

https://doi.org/10.5194/egusphere-2026-2734
Preprint. Discussion started: 11 June 2026

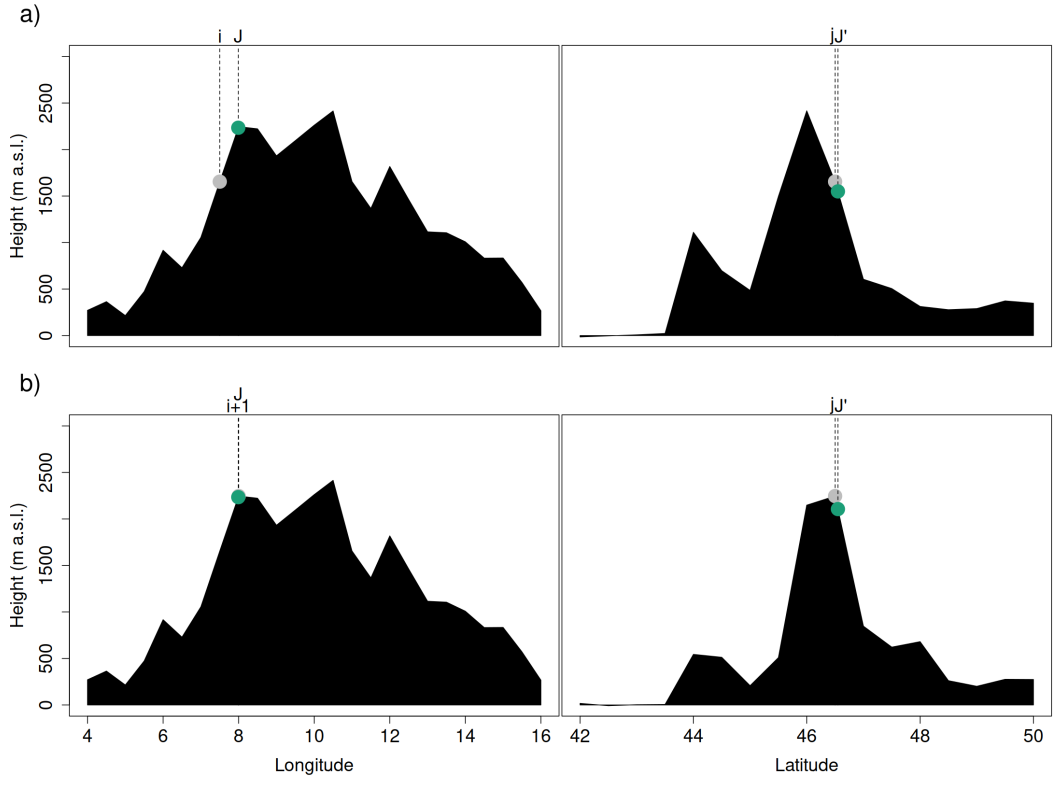

Figure 3. Cross sections of ERA5 0.5°×0.5° orography at JFJ station along longitude and latitude at a) grid point (i,j) and b) eastward grid point (i+1,j). The grey dot indicate the calculated grid cell indices of the JFJ actual location (indicated in green).

https://doi.org/10.5194/egusphere-2026-2734
Preprint. Discussion started: 11 June 2026

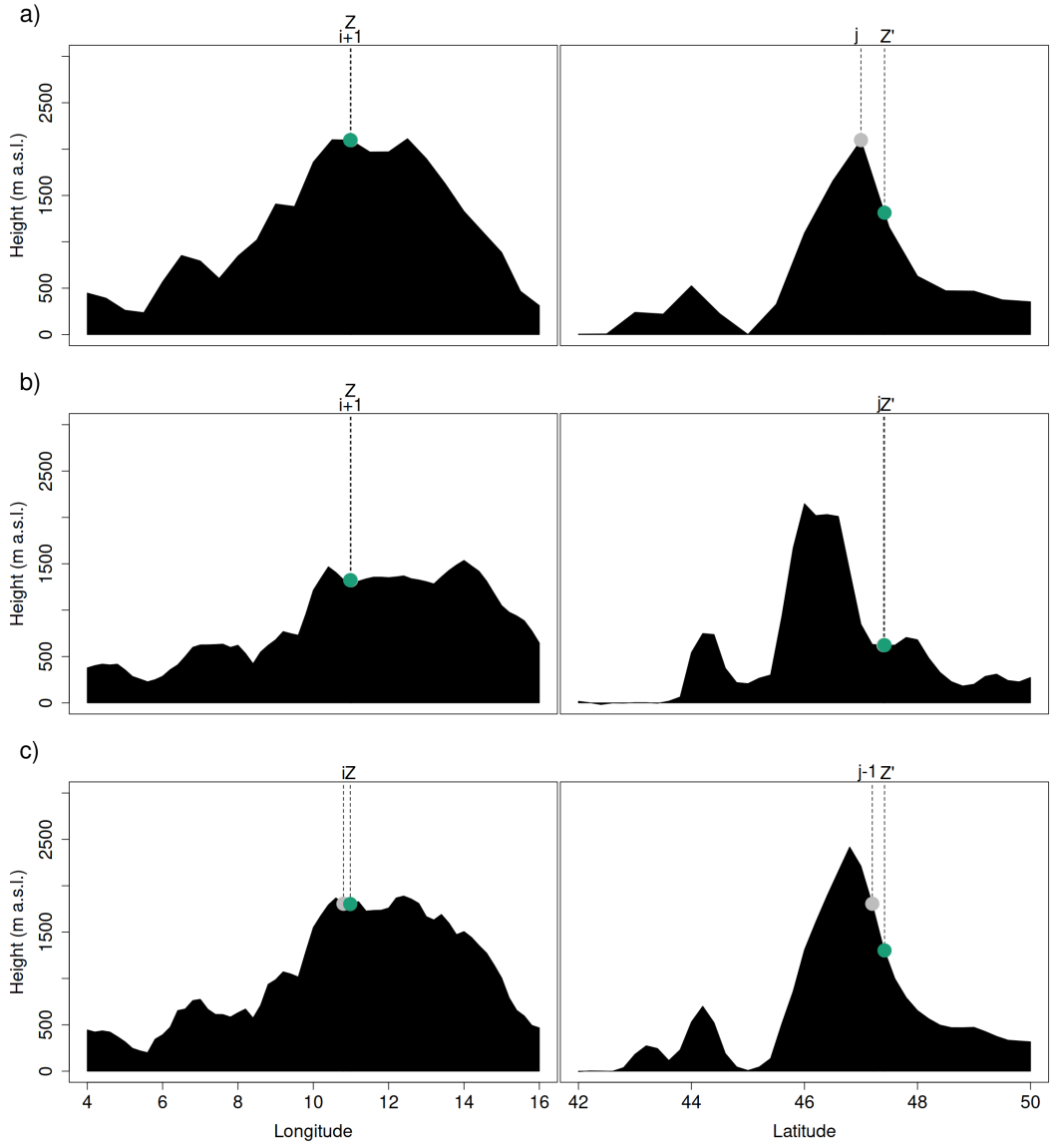

Figure 4. Cross sections of ZSF station orography along longitude and latitude at a) ERA5 $0.5° \times 0.5°$ grid point $(i+1, j)$, b) ERA5 $0.2° \times 0.2°$ $(i+1, j)$, and c) southward grid point $(i, j-1)$. The grey dot indicate the calculated grid cell indices of the ZSF actual location (indicated in green).

https://doi.org/10.5194/egusphere-2026-2734
Preprint. Discussion started: 11 June 2026

A mismatch was observed at ZSF at a finer spatial resolution, where the actual coordinates of ZSF (Fig. 2b, green dot) was located at the eastward grid point $(i+1, j)$ at a low orography height of 1322.41 m (Fig. 4b), which was significantly lower than the height at the grid point $(i+1, j)$ at coarser resolution, namely at 2096.70 m (Fig. 4a). We would expect that the orography height would be higher at finer spatial resolution. The southern grid point $(i, j-1)$ was located at a slightly higher altitude of 1805.64 m and the cross section of the mountain resembles that at coarser resolution (Fig. 4a). Therefore, $\theta_{\text{ERA5,ZSF}}$ and T-rh was calculated from this grid point for the model runs using the $0.2° \times 0.2°$ wind fields.

2.4 Atmospheric Inversion

The concepts of atmospheric inverse modeling date back around four decades (Tarantola and Valette, 1982) and is mathematically described by a cost function that quantifies the misfit between two states, the a priori state $J_p(\mathbf{x})$ and the observational state $J_y(\mathbf{x})$, and seeks a state variable that minimizes the cost function, resulting in a posterior estimate $\mathbf{x}$ providing the best fit to both observations and the prior information i.e., the gridded emissions of SF_6 in kg m^{-2} s^{-1} (Eq. 4). This considers also uncertainties assigned to the prior information and observations.

We applied the open-source Bayesian FlexInvert tool (https://flexinvert.nilu.no), suitable for solving linear inverse problems and designed to optimize surface fluxes of GHG species and aerosol based on ground-based and satellite measurements (Thompson and Stohl, 2014). We applied a Quasi-Newton optimization method (the M1QN3 algorithm in FlexInvert) (Eq. 5), which considers a log-normal probability distribution function (PDF) for the prior emission errors and the posterior emissions, $\mathbf{x}$, are those corresponding to the median of the posterior PDF (Thompson et al., 2025). This works well when emissions (and prior errors) do not follow a normal distribution, such is the case for SF_6 and many atmospheric compounds (Seinfeld and Pandis, 2016). We run 30 iteration to ensure that the model reaches a minimum and we find the solution corresponding to the median of the PDF.

$$J(\mathbf{x}) = \frac{1}{2}(J_p(\mathbf{x}) + J_y(\mathbf{x})) \tag{4}$$

$$J(\mathbf{x}) = \frac{1}{2}(\ln(\mathbf{x}) - \ln(\mathbf{x_0}))^\top \mathbf{B}^{-1}(\ln(\mathbf{x}) - \ln(\mathbf{x_0})) + \frac{1}{2}(\mathrm{H}(\mathbf{x}) - \mathbf{y})^\top \mathbf{R}^{-1}(\mathrm{H}(\mathbf{x}) - \mathbf{y}) \tag{5}$$

FLEXPART is used to relate changes in fluxes to changes in dry mole fractions, that is, to derive the transport operator $\mathrm{H}(\mathbf{x})$. Observational information $\mathbf{y}$ provides a constraint on surface fluxes $\mathbf{x}$, while the a priori emission vector $\mathbf{x_0}$ regularizes the under-constrained problem and represents our best estimate (based on bottom-up emissions) before the observations. However, the constraints of observations $\mathbf{y}$ and prior emissions $\mathbf{x_0}$ need to be weighted, respectively, by the observation error (including model representation error) as described by the observation error covariance matrix, $\mathbf{R^{-1}}$ and the prior error, as described by the prior error covariance matrix, $\mathbf{B^{-1}}$. The posterior emission, $\mathbf{x}$, is the vector which minimizes the cost function and is the

https://doi.org/10.5194/egusphere-2026-2734
Preprint. Discussion started: 11 June 2026

optimal estimate of the state (Tarantola, 2005). The SF_6 emission estimate from EDGARv8 was used as independent a priori information in this inversion.

Table 4. FlexInvert configuration.

N° inversions	N° regions	Nested domain	Prior fluxes	Obs unc	Min prior
Sampling	1503	4°–16°E,	EDGARv8	0.06 ppt	10^{-13}
Proxy	1608	42°–50°N	optimized SF_6 fluxes		$kgm^{-2}h^{-1}$
Theta	1584	$0.1° \times 0.1°$	(Vojta et al., 2024, 2025)		

In the atmospheric inversion, an aggregated grid with variable resolution is applied for the nested domain, with the finest horizontal grid resolution of $0.1°\times0.1°$, followed by a coarser grid elsewhere and is based on the SRR fields to limit computational cost (Thompson and Stohl, 2014) and an example aggregated grid based on T-rh SRR fields is given in Appendix A5. The transport is calculated at the same resolution as the SRRs, but the control (or equivalent, state) vector is defined on an aggregated grid. We apply a temporal resolution of one month and a temporal correlation of

2.5 Sensitivity tests

Two prior SF_6 fluxes were used in forward simulations, based on the SRR fields, to obtain SF_6 mixing ratios: EDGARv8 (EDGAR et al., 2023) at $0.1°\times0.1°$ grid resolution and optimized European SF_6 fluxes estimated by Vojta et al. (2025, 2024) at $0.25°\times0.25°$ grid resolution that was re-gridded to the model domain of $0.1°\times0.1°$. They were evaluated against observations using various statistical metrics to explore variability, correlation, bias, and error (Table 5) for all receptor sites in three scenarios: S-rh, P-rh, and T-rh. The statistical metrics are calculated for three-hourly averaged time series, day (11:00-15:00 UTC) and night (23:00-03:00 UTC) hourly observations, and for the seasons. Four statistical metrics are listed (Table 5): Pearson correlation (R), centered root mean square error (cRMSE), Mean Bias Error (MBE), and normalized standard deviation (σ_n). Small differences were observed between the two prior fluxes and therefore the error statistics is only presented for simulated SF_6 priors using EDGARv8 and wind fields at two horizontal resolutions ($0.5°\times0.5°$ and $0.2°\times0.2°$) at various release heights for JFJ, ZSF, and SSL. The statistics were graphically summarized in the form of Taylor diagrams to illustrate the similarity of the various release heights (indicated by different shapes) and by seasons (indicated by different outline colours of the shapes), and how well they match SF_6 observations, considering variability, correlation, error, and bias. The MBE was added to the Taylor diagrams as a color scale.

Wind speed and wind direction were analysed from the ERA5 model to identify time windows where the model did not perform as expected and to better understand the choice of particle release height in simulated time series.

https://doi.org/10.5194/egusphere-2026-2734
Preprint. Discussion started: 11 June 2026

Table 5. Error statistics of RMSE, MBE and R. P_i represents prior simulate mixing ratios and O_i represents the observations.

Metrics	Name	Mathematical expressions
Centered Root Mean Square Error	cRMSE	$\sqrt{\frac{1}{N}\sum_{i=1}^{N}\left[(P_i-\overline{P})-(O_i-\overline{O})\right]^2}$
Mean Bias Error	MBE	$\frac{1}{N}\sum_{i=1}^{n}(P_i-O_i)$
Pearson correlation coefficient	R	$\frac{\sum_{i=1}^{n}(P_i-\bar{P})(O_i-\bar{O})}{\left\{\sum_{i=1}^{n}(P_i-\bar{P})^2\sum_{i=1}^{n}(O_i-\bar{O})^2\right\}^{\frac{1}{2}}}$
Normalized Standard Deviation	σ_n	$\frac{\sqrt{\frac{1}{N}\sum_{i=1}^{n}(P_i-\overline{P})^2}}{\sqrt{\frac{1}{N}\sum_{i=1}^{n}(O_i-\overline{O})^2}}$

3 Results and discussion

The performance of simulated priors at various release heights, at different times of the day and seasons, and with wind fields at two different spatial resolutions are illustrated in Taylor diagrams Fig. 5−7.

For the high mountain station JFJ (Fig. 5), which is predominantly in the free troposphere throughout the year, the Taylor diagrams demonstrated a clear dependence of the performance on the release height choice and on the seasonality for the coarser resolution wind fields (Fig. 5a-c). Considering all observations, JF and MAM scores were clustered closest to the observed variability (σ_n), and T-rh scores were lying between P-rh (highest σ_n) and S-rh (lowest σ_n) and exhibited a lower error (cRMSE) and bias (MBE) than P-rh and marginally stronger correlation (R). While in summer (JJA), only a very small fraction of observed σ_n was explained and the scores where grouped closely together, although S-rh presented a negative MBE in comparison to T-rh and P-rh. During SON, the scores explained only about half of the observed σ_n, but T-rh demonstrated a lowest MBE. At daytime hours, small differences between the release heights were observed, although S-rh explained somewhat more the observed σ_n for JF, MAM, and SON. The seasonal scores seemed to be less dependent of the release height choice during daytime and were distinguished only during SON, where T-rh was more similar to P-rh and exhibited a lower MBE than S-rh. The overall pattern of JF and MAM scores showed a stronger R during daytime hours, while JJA and SON scores demonstrated stronger R during nighttime. The release height differences were greater during nighttime hours, and T-rh showed the overall best performance for JF, MAM, and SON. In summer, S-rh demonstrated stronger R, lower cRMSE and MBE. At higher resolution wind fields (Fig. 5d-f), the scores of the release heights showed greater differences. Considering all hours of the day, T-rh produced less observed σ_n than P-rh in JF, but greater σ_n than S-rh, and demonstrated a reduced cRMSE, MBE, and stronger R than P-rh in both JF and MAM. In SON, P-rh demonstrated strongest R, lowest cRMSE, and MBE for all hours of the day and during daytime a higher σ_n was observed, while T-rh showed a better performance than S-rh. During

https://doi.org/10.5194/egusphere-2026-2734
Preprint. Discussion started: 11 June 2026

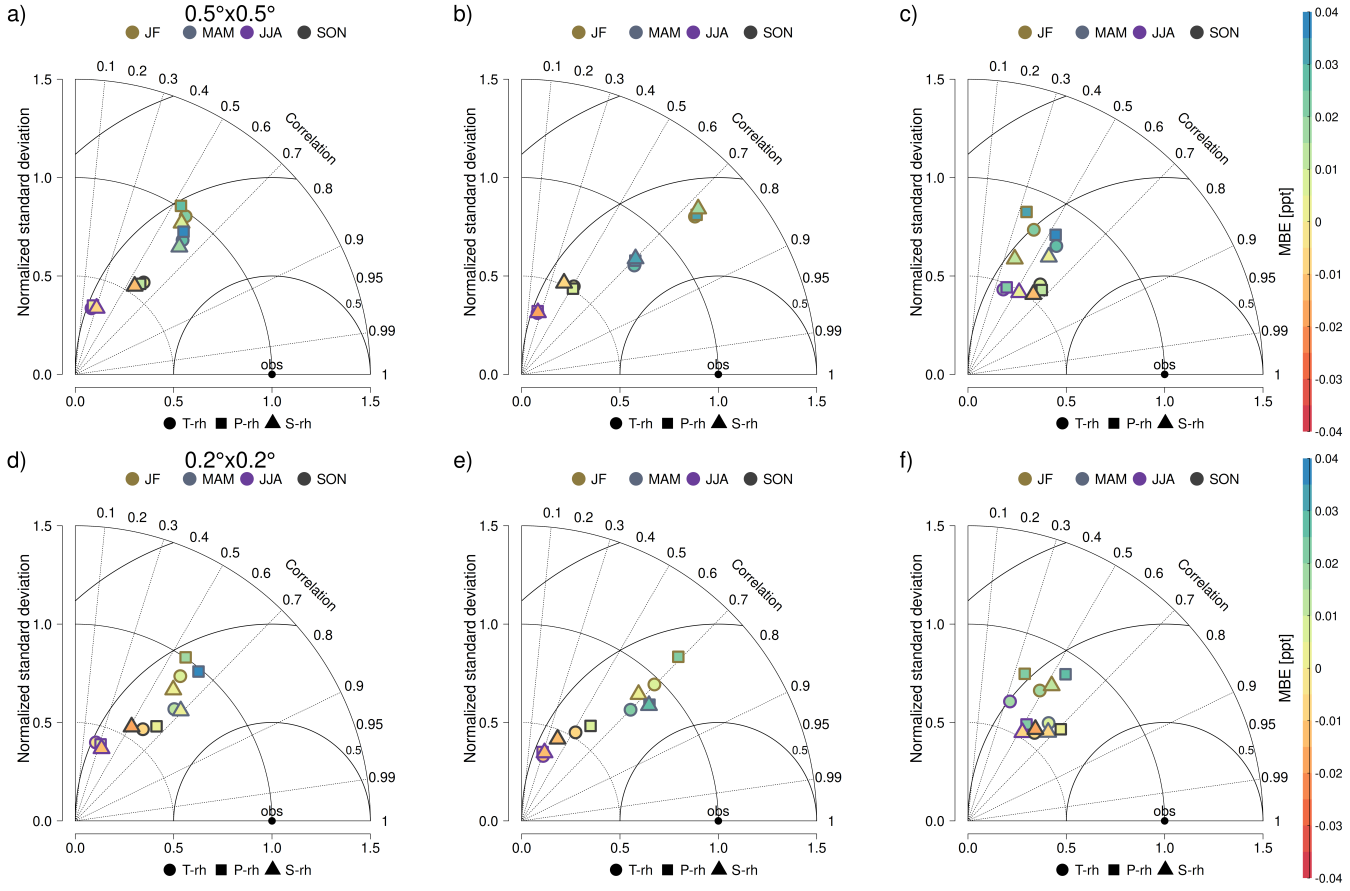

Figure 5. Taylor diagrams for the simulated SF_6 mixing ratios JFJ station across all release height scenarios and seasons. The error statistics were calculated based on a-d all observations; b-e daytime hours; c-f nighttime hours. Panel a-c was based on ERA5 wind fields at $0.5^\circ \times 0.5^\circ$ spatial resolution, and panel d-f $0.2^\circ \times 0.2^\circ$ resolution.

nighttime hours, P-rh produced highest σ_n and a positive MBE in JF and particularly during MAM ($\approx 0.04 - 0.05$ ppt), while T-rh showed a lower MBE and σ_n, but stronger R and was more similar to S-rh. In summer (JJA), T-rh showed greatest σ_n and reduced MBE, but weaker R and higher cRMSE in comparison to T-rh. During SON, strongest correlation was observed for P-rh as well as lowest MBE.

Among all seasons and hours of the day and considering both spatial resolutions, T-rh demonstrated in general a good performance, in particular during JF and MAM, while the worse performance was observed during summer months.

For the ZSF station applying coarser resolution wind fields (Fig. 6a-c), the release heights showed very similar scores clustered together by season, except for JF, where T-rh and P-rh gave higher σ_n than S-rh, which exhibited a negative MBE. During daytime hours, MAM showed strongest correlation and lower cRMSE and during SON, highest σ_n and lowest MBE was observed. Considering only nighttime hours, T-rh was overall more similar to P-rh except for JF, where T-rh demonstrated

https://doi.org/10.5194/egusphere-2026-2734
Preprint. Discussion started: 11 June 2026

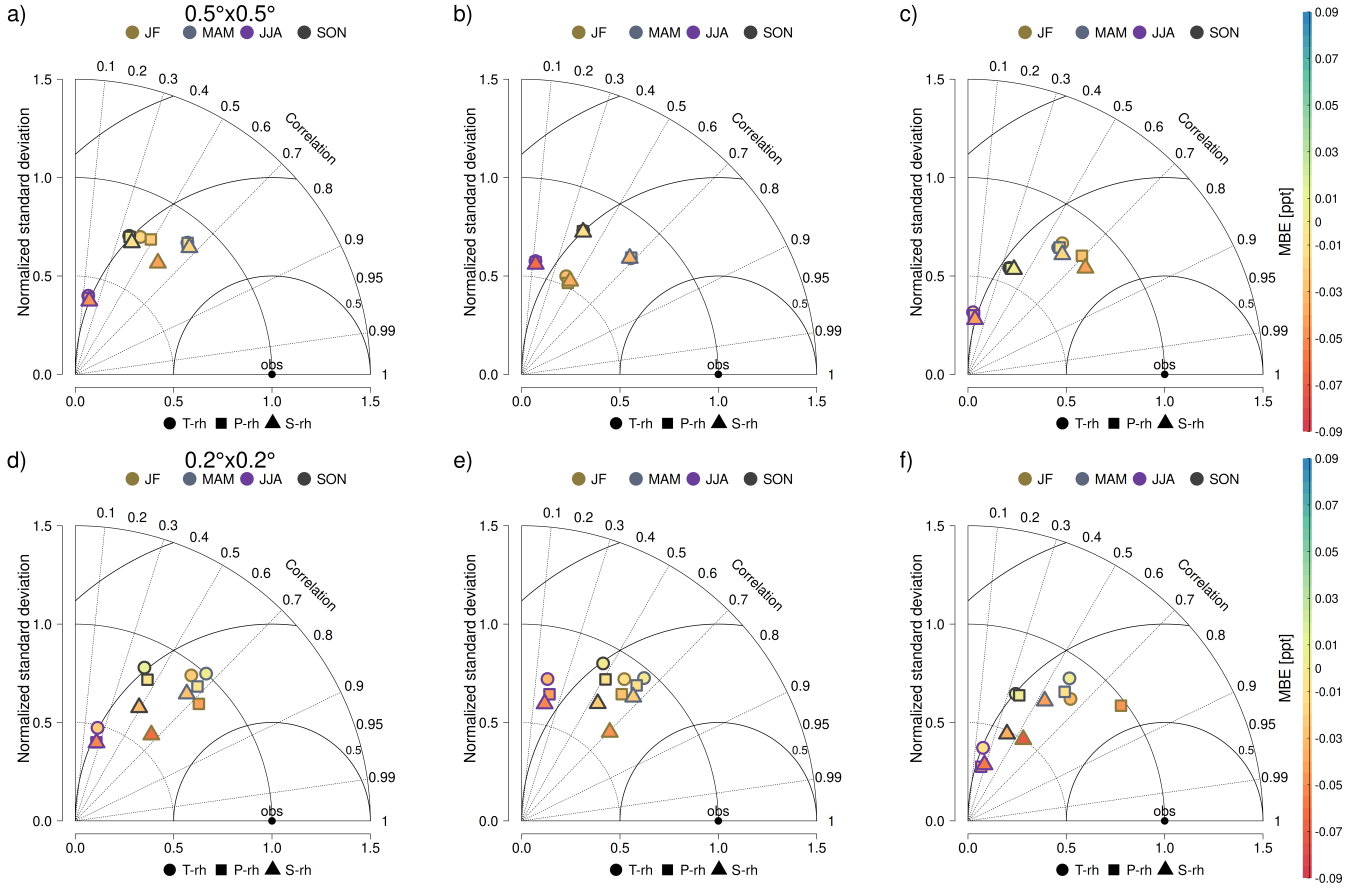

Figure 6. Taylor diagrams for the simulated SF_6 mixing ratios across all release height scenarios and seasons at the ZSF station. The error statistics were calculated based on a-d all observations; b-e daytime hours; c-f nighttime hours. Panel a-c was based on ERA5 wind fields at $0.5^\circ \times 0.5^\circ$ spatial resolution, and panel d-f $0.2^\circ \times 0.2^\circ$ resolution.

higher σ_n, but weaker R and higher cRMSE. S-rh consistently produced lower σ_n values for all seasons and negative MBE for JF, MAM, and JJA, indicating a weaker overall performance. In general, the strongest R and lowest cRMSE was observed for JF and MAM, although SON showed smaller MBE and higher σ_n. All three scenarios showed similar scores, which could suggest that the wind and mixing are not significantly different across the model levels for the release height scenarios, resulting in almost identical transport pathways.

At higher resolution wind fields (Fig. 5d-f), all release height scenarios showed greater spread of scores and divergence from one another. When evaluating all hours of the day, T-rh demonstrated the greatest σ_n for all seasons and lowest MBE, while S-rh captured poorly the σ_n and exhibited a negative MBE. During daytime hours, T-rh showed an overall good performance with highest σ_n and lowest MBE. T-rh scores were closer to P-rh throughout the seasons, while S-rh consistently had the lowest σ_n and a negative MBE. In JF during nighttime, the pattern changed, and P-rh yielded the highest R and lowest cRMSE and

https://doi.org/10.5194/egusphere-2026-2734
Preprint. Discussion started: 11 June 2026

showed the best agreement with observations, however T-rh showed a lower MBE and overall better performance than S-rh. In MAM and JJA, T-rh represented the observed σ_n best, and exhibited a lower MBE than both P-rh and S-rh, although less than 50 % of σ_n was being accounted for in JJA. In SON, T-rh showed highest σ_n and was very similar to P-rh, although with a slightly more positive MBE than P-rh. Overall for T-rh, higher σ_n values were observed during daytime, whereas at night, lower cRMSE and less negative MBE values were obtained. In contrast, S-rh showed consistently lowest σ_n and tended to underestimate observed variability, while P-rh scores were situated between T-rh and S-rh. T-rh showed overall the best performance at ZSF at finer spatial resolution, effectively capturing observed variability during both daytime and nighttime, while maintaining comparable cRMSE and MBE.

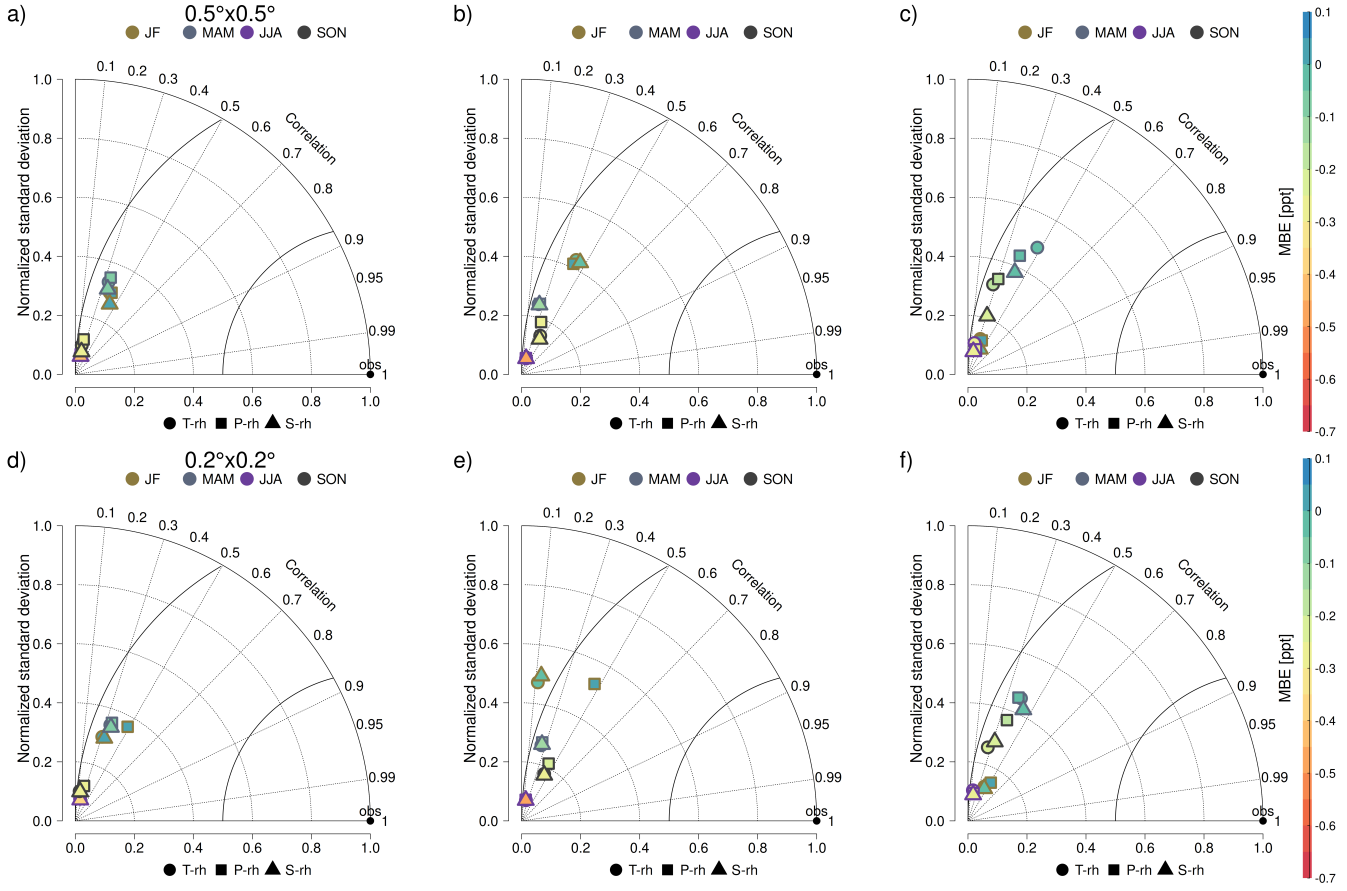

Figure 7. Taylor diagrams for the simulated SF_6 mixing ratios across all release height scenarios and seasons at the SSL station. The error statistics were calculated based on a-d all observations; b-e daytime hours; c-f nighttime hours. Panel a-c was based on ERA5 wind fields at $0.5° \times 0.5°$ spatial resolution, and panel d-f $0.2° \times 0.2°$ resolution.

The SSL station differ from the other station due to its lower altitude and is more influenced by the ABL dynamics. The Taylor diagrams of SSL station (Fig. 7) showed the strongest contrast among all stations, but this is likely due to the offset

https://doi.org/10.5194/egusphere-2026-2734
Preprint. Discussion started: 11 June 2026

in simulated mixing ratios (explained in Sect xxx) resulting in very low observed variability and weak correlation (R > 0.5). The top diagrams (Fig. 7a-c) using coarser-resolution wind fields showed that the scores generally under-represented observed variability and only JF and MAM accounted for some σ_n. During daytime, scores were very similar except for SON, where P-rh showed highest σ_n, and T-rh was more similar to S-rh. During nighttime, JF and JJA showed negligible σ_n, while T-rh demonstrated best performance during MAM (highest σ_n and greatest R), and during SON T-rh was similar to P-rh, which exhibited a slightly higher σ_n values. Overall, T-rh resulted in a better performance during nighttime and S-rh showed overall the poorest performance (lowest σ_n and weak R). No significant difference was observed in the MBE values for the various release height scenarios, but during daytime, more positive MBE was observed during JF and MAM, while JJA showed negative MBE, and SON showed MBE values closer to zero. At higher resolution wind fields (Fig. 7d-f), P-rh achieved the best performance during JF, predominantly under daytime conditions (strongest R, highest σ_n, and a positive MBE), while T-rh showed poor performance (weakest R and highest cRMSE) and was more similar to S-rh. During nighttime, T-rh and P-rh produced highest σ_n for MAM and P-rh showed highest σ_n during SON, whilst T-rh and S-rh scores were more similar. In JJA, all scores were clustered near zero variance at both spatial resolutions and at all times of the day, with a negative bias and overall poor performances. This was likely due to the very high variability in observed SF_6 mixing ratios that was not well captured in the simulated mixing ratios for the various release heights. Overall, T-rh and P-rh did simulate the observations better than S-rh at MAM and SON and during nighttime hours.

3.1 Comparison of simulated time series across release height scenarios

Spurious increases in the simulated SF_6 mixing ratios occurred at ZSF during the period `18-01-2019` to `23-01-2019` (Fig. 8a), only when using EDGARv8 as prior fluxes and ERA5 at $0.5° \times 0.5°$ resolution. This confirms the significant influence of prior fluxes with different horizontal resolution wind fields on simulated SF_6 mixing ratios (Fig. 8b) and also depends on the prior fluxes used (Fig. 8a) and the choice of particle release height, as the highest release height (in this case S-rh) and typically higher than the MLH and thus does not erroneously pick up emission signals During this same period, a very low mixing height (MLH) occurred (Fig. 8b), probably leading to stagnation and little to no mixing/dispersion of emissions. The observed pollution peak on `2019-01-25 01:00` is successfully simulated by all three release height scenarios. The SRR maps in Fig. 9 show similar sensitivities, although T-rh is below MLH and near the orography at the ZSF site, where also weak horizontal winds are observed.

https://doi.org/10.5194/egusphere-2026-2734
Preprint. Discussion started: 11 June 2026

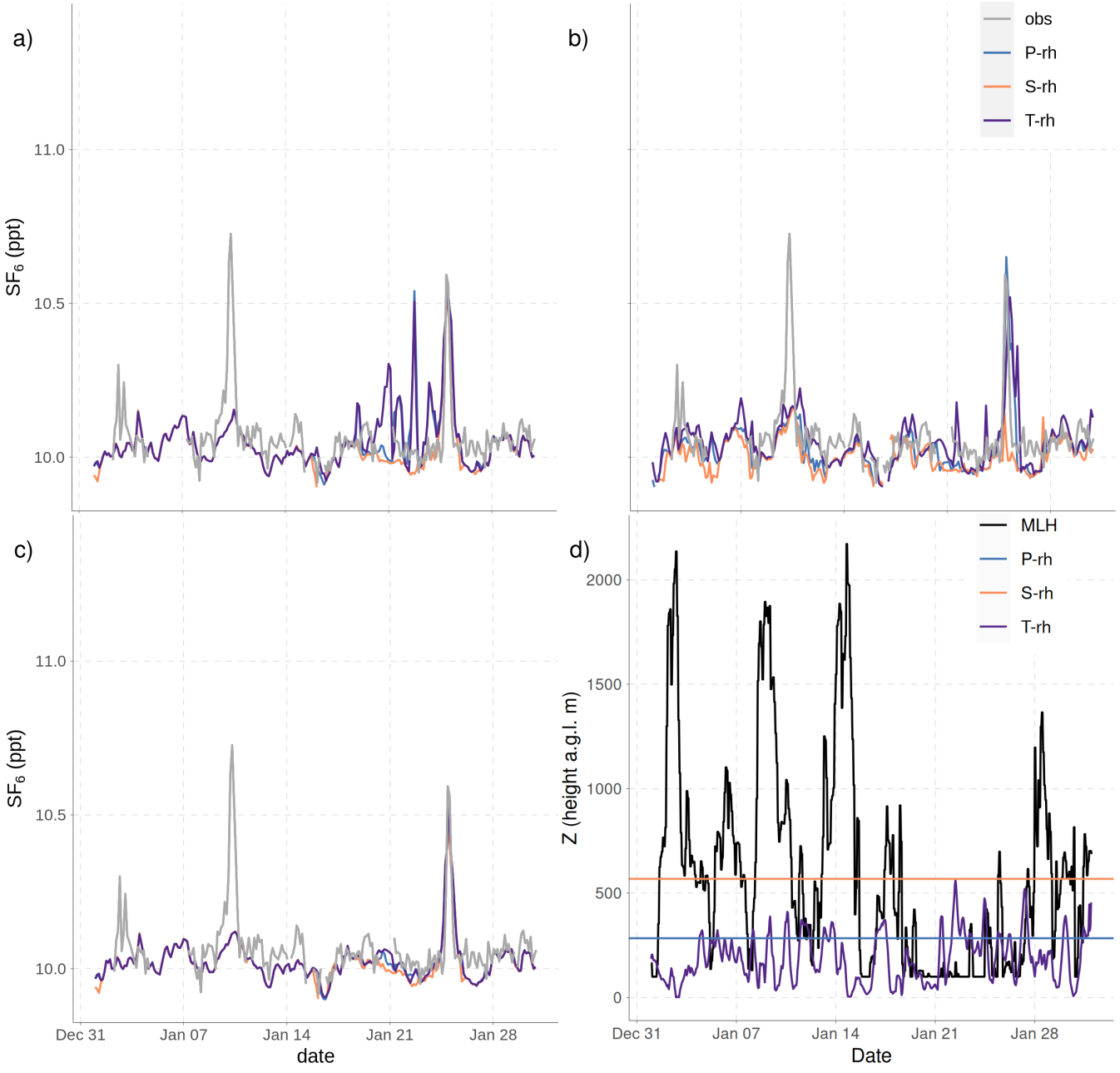

Figure 8. 3-hourly simulated SF_6 mixing ratios at ZSF (Jan 2019): using EDGARv8 and ERA5 at a) 0.5° ×0.5°, b) at 0.2° ×0.2°, c) using optimized prior and ERA5 at 0.5° ×0.5°, and d) mixing layer height (MLH) and the three release heights.

https://doi.org/10.5194/egusphere-2026-2734
Preprint. Discussion started: 11 June 2026

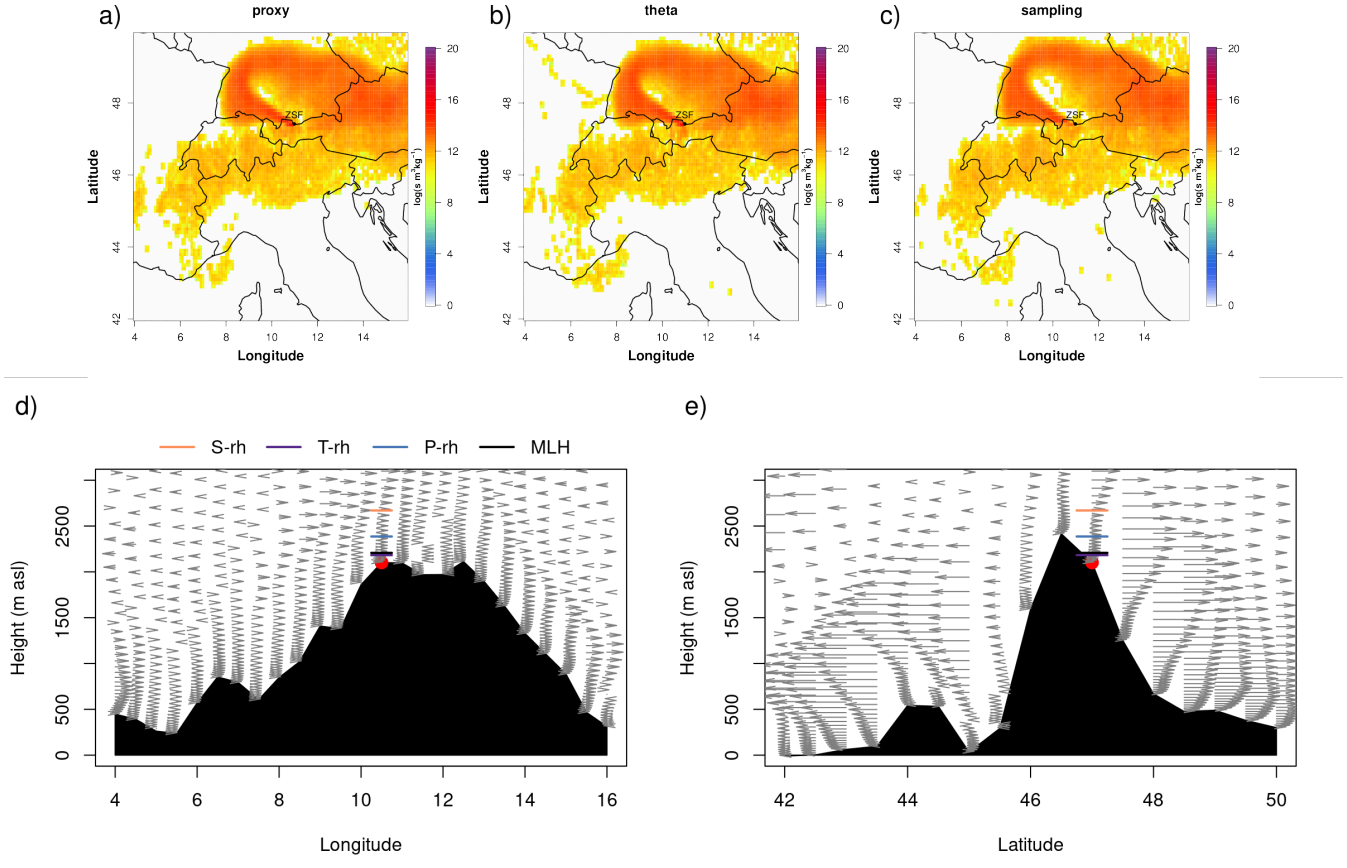

Figure 9. SRR maps of a) P-rh, b) T-rh, c) S-rh, d) a zonal cross section of uu winds, and e) a meridional cross section for vv winds on `2019-01-25 01:00`. The ZSF site is indicated as a red dot.

https://doi.org/10.5194/egusphere-2026-2734
Preprint. Discussion started: 11 June 2026

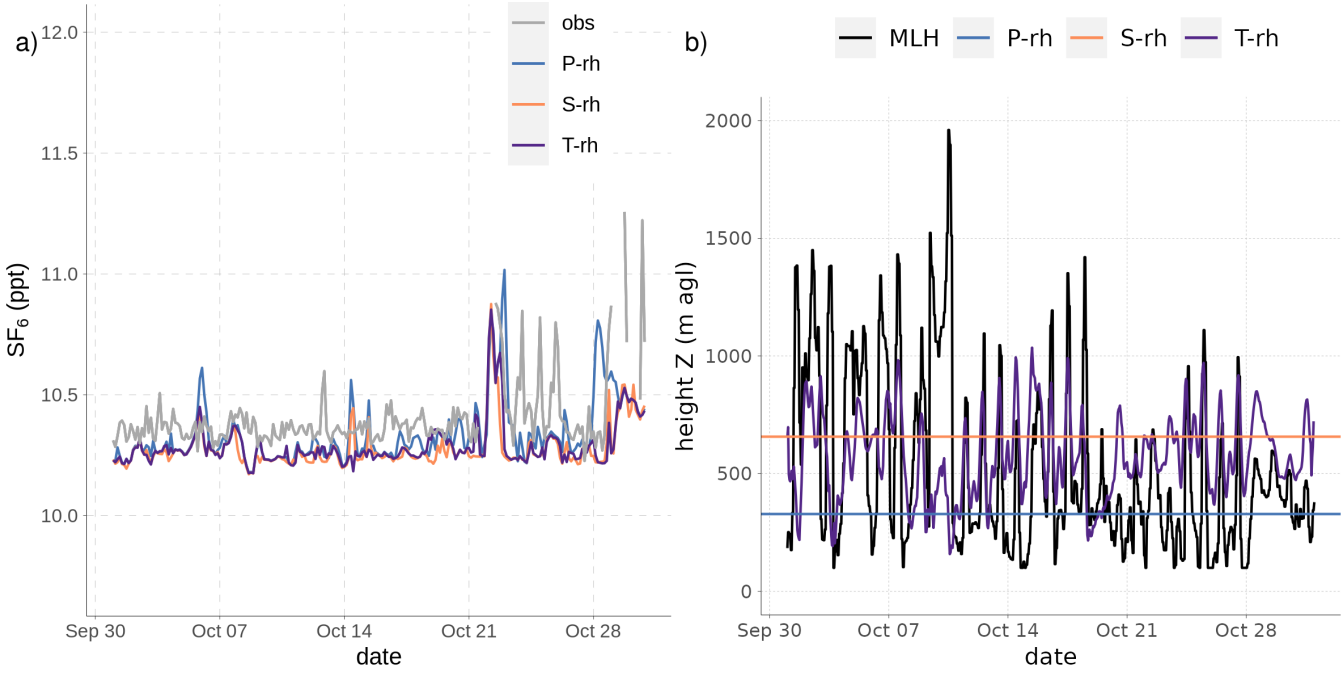

Figure 10. Simulated SF_6 mixing ratios at SSL in Oct 2019 using a) optimized prior emissions and wind fields at $0.5° \times 0.5°$ spatial resolution, and b) mixing layer height (MLH) and the three release height scenarios.

We examined a case in which simulated SF_6 prior mixing ratios at SSL using various release heights underestimated three observed SF_6 pollution events during the period `2019-10-24` to `2019-10-25` (Fig. 10). The cross section of zonal winds on the `2019-10-23 23:00` (Fig. 11d) shows a convergence zone near the receptor site where the intensity of the wind decreases with height. The differences in SRRs are therefore predominantly influenced by the difference in release heights, i.e., P-rh being close to the MLH and significantly lower than those of T-rh and S-rh, resulting in higher sensitivity and mixing ratios for the P-rh scenario. In general, the wind analysis shows a familiar pattern: a low mixing layer height during the night, low wind intensity, and higher simulated mixing ratios at lower release heights. When MLH reaches its minimum, we observe very high sensitivity and stagnant air, leading to higher SF_6 mixing ratios across all release height scenarios, particularly at lower release heights.

https://doi.org/10.5194/egusphere-2026-2734
Preprint. Discussion started: 11 June 2026

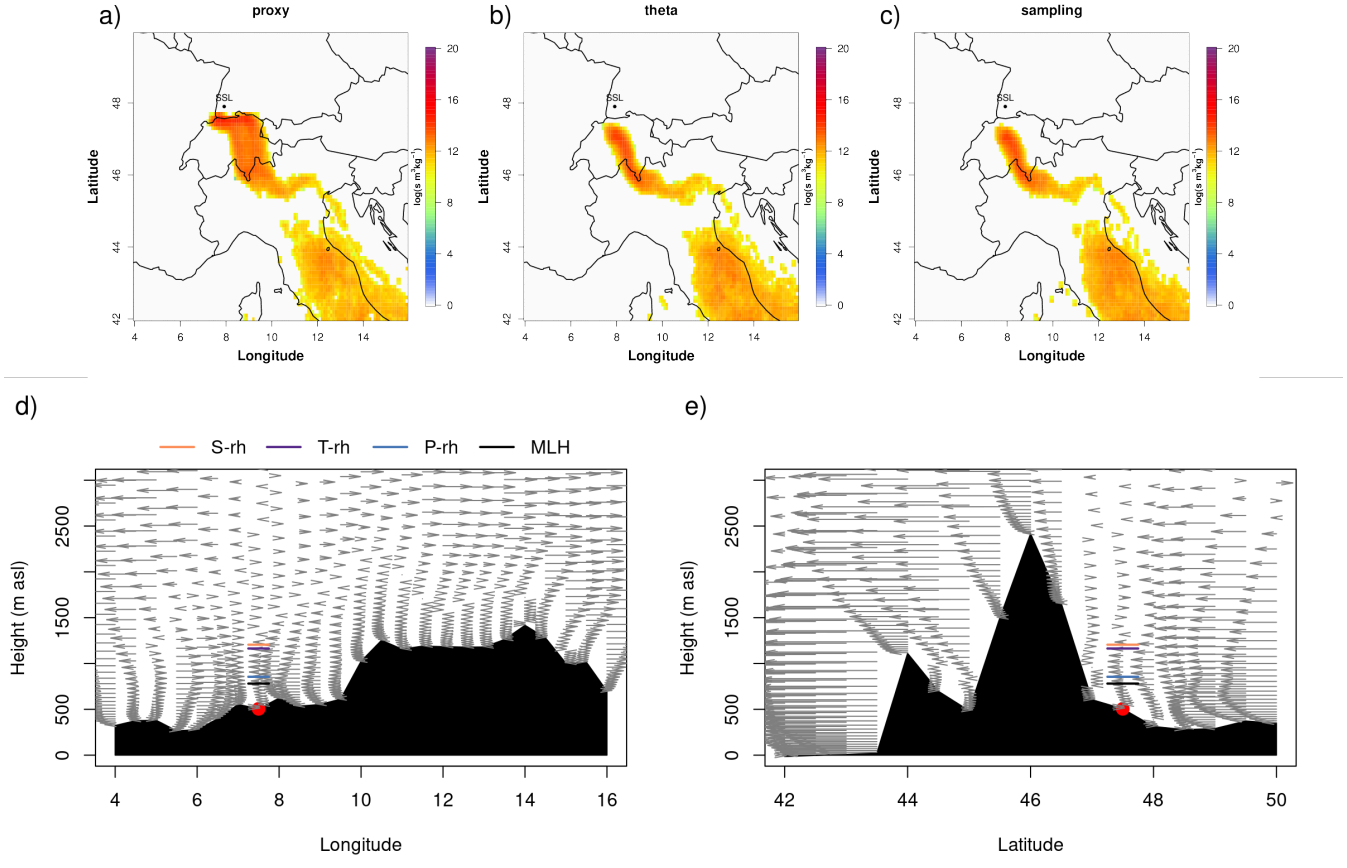

Figure 11. SRR maps of a) P-rh, b) T-rh, c) S-rh, d) a zonal cross section of uu winds, and e) a meridional cross section for vv winds on `2019-10-23 23:00`. The SSL site is indicated as a red dot.

https://doi.org/10.5194/egusphere-2026-2734
Preprint. Discussion started: 11 June 2026

3.2 Inversion results

The results of the atmospheric inversions are presented in Fig. 12 shows the increment i.e. the difference between posterior (fpos) and prior (fpri) fluxes of the nested domain is expressed as flux increment. The total increment is given in Table 6 for the three release height scenarios, using ERA5 wind fields at two spatial resolution.

The inversion results using coarser resolution wind fields (Fig 12a-c) showed that the release height choice significantly influence the posterior flux distribution, in which P-rh and T-rh resulted in an overall larger negative flux increment than S-rh. In particular near the mountain receptor ZSF and SSL, largest negative flux increment was observed at T-rh, while near JFJ, the greatest negative increment was observed at P-rh and was less pronounced at S-rh. In the Po valley region, a significant positive flux increment was observed for P-rh and T-rh and a smaller negative flux increment in Piedmont region that was also observed at S-rh. Given that S-rh releases particles at higher altitudes, a reduced SRR sensitivity was expected and larger posterior fluxes to match observed mixing ratios. This response was observed in Germany and near SSL site and hence S-rh yielded a lower total negative flux increment in comparison to P-rh and T-rh.

At higher resolution wind fields (Fig 12d-f), S-rh produced even higher posterior emissions in southern Germany near SSL receptor to match the observed mixing ratios, while P-rh and T-rh produced significantly more negative fluxes around SSL. Again this suggests that the choice of release height influences the particle trajectory and consequentially the MDM introduced in the inversion, resulting in erroneous posterior fluxes (in this case, the MDM at SSL site explained in Sect. 2.2.1). Also, a significant negative flux increment occurred in Piedmont region in northern Italy at S-rh and some positive increment towards the centre of the Po valley, meanwhile T-rh showed only small increment in this region. Overall, more negative total posterior fluxes are observed at T-rh in particular in southern Germany near ZSF receptor.

The comparison of the release heights at the two spatial resolutions, showed that T-rh significantly influenced the posterior flux distribution relative to the prior especially at finer spatial resolution where T-rh resulted in a decrease of 2.3 % in posterior emissions, while S-rh resulted in a decrease of 0.73 %. This means, that the inversion is highly sensitive to the model-data mismatch, and choosing a inappropriate release height e.g. S-rh can result in systematic biases of posterior fluxes, especially at sites like SSL.

Table 6. Total increment for year 2019 over the nested domain for the three release height scenarios using ERA5 wind fields at two spatial resolution

	P-rh [$\mathrm{Tgy^{-1}}\cdot10^{-5}$]	**T-rh** [$\mathrm{Tgy^{-1}}\cdot10^{-5}$]	**S-rh** [$\mathrm{Tgy^{-1}}\cdot10^{-5}$]
Prior		9.4449	
$\mathrm{Increment}_{\mathbf{ERA5}\,0.5^\circ\times0.5^\circ}$	-0.1861	-0.1472	-0.1338
$\mathrm{Increment}_{\mathbf{ERA5}\,0.2^\circ\times0.2^\circ}$	-0.1567	-0.2142	-0.0688

https://doi.org/10.5194/egusphere-2026-2734
Preprint. Discussion started: 11 June 2026

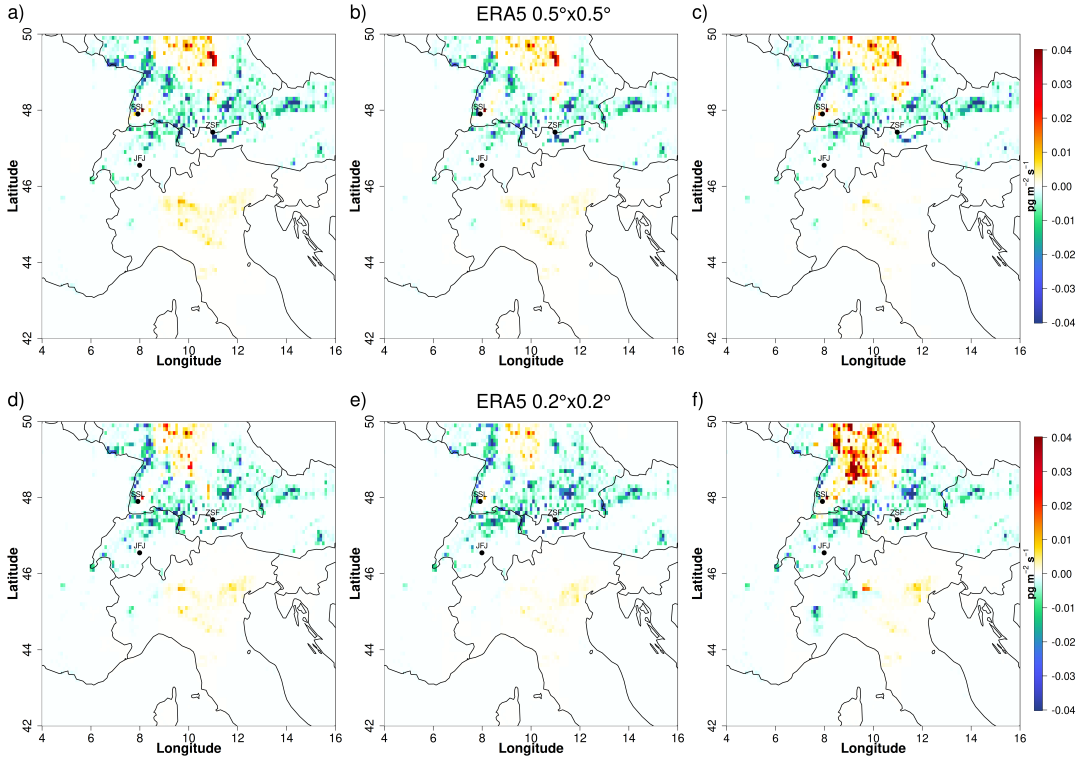

Figure 12. Total flux increment for 2019 of a-d) P-rh, b-e) T-rh, and c-f) S-rh using ERA5 $\mathbf{0.5}^\circ \times \mathbf{0.5}^\circ$ and $\mathbf{0.2}^\circ \times \mathbf{0.2}^\circ$ horizontal resolution.

https://doi.org/10.5194/egusphere-2026-2734
Preprint. Discussion started: 11 June 2026

4 Conclusion

This research applied the Bayesian atmospheric inverse modeling framework FlexInvert coupled with FLEXPART driven by the ECMWF ERA5 reanalysis product, and tested at two different horizontal grid resolutions of $0.5° \times 0.5°$ and $0.2° \times 0.2°$ to more rigorously assess their impact on simulated mixing ratios over the nested domain covering Northern Italy, 4°E–16°E, 42°–50°N, at $0.1° \times 0.1°$ spatial resolution.

We addressed the challenges in accurately representing mountain receptors in atmospheric transport models driven by coarse resolution meteorological fields by introducing a new approach for determining the optimal release heights using potential temperature. In FLEXPART, three different release height scenarios were examined: (i) virtual particles are released from the station sampling inlet height (S-rh), ii) a fixed intermediate point release between ERA5 model orography and station sampling height (P-rh), iii) and a varying release height based on matching ERA5 potential temperature with observations (T-rh). The release height were tested at the three mountain sites: Jungfraujoch (JFJ), Zugspitze (ZSF), and Schauinsland (SSL) using using SF_6 as a tracer. Evaluation of the modeled atmospheric transport at the three sites demonstrated that both the spatial resolution of the meteorological fields and the release height choice strongly impacted the simulated mixing ratios and did depend on the specific mountain site, the time of day, and the season. Wind speed and wind direction were analysed from the ERA5 model to identify time windows where the model did not perform as expected and to better understand the choice of particle release height in simulated SF_6 mixing ratios across the sites using two prior fluxes. The simulated SF_6 mixing ratios driven by a coarser resolution wind field showed similar performance across all three release height scenarios, with overall scores clustering closely together. Applying higher resolution wind fields generally enhanced the differences between the various release heights scenarios, especially under nighttime conditions, resulting in an improved representation of the atmospheric transport and better model-data agreement using T-rh approach at ZSF and JFJ. The varying release height, T-rh, reproduced well the observed variability and overall, delivered a consistent performance at all mountain sites. Nevertheless, the model performance was weakest during summer, highlighting the challenges in representing ABL processes in the ATM. This approach was also limited at SSL station, due to a discrepancy between the simulated mixing ratios and observations leading to a higher model-data mismatch. In addition, SF_6 inversion results showed that using a higher release height (S-rh) typically led to smaller source-receptor sensitivity of the mountain receptor and to compensate, led to a higher posterior flux estimate near SSL site, highlighting the importance of selecting an appropriate release height.

Further methodological development is required to validate and test the varying release height approach using higher resolution wind fields and at other mountain stations using other tracers i.e. HFC-134a, which is monitored at several mountain stations and for which the emission sources are well characterized. The findings of this study lay the groundwork for future research to develop a method applicable at all seasons and at different mountains. Although the FLEXPART configuration provided a robust framework for simulating SRRs at mountain stations, we acknowledge that relying on ERA5 wind fields with relatively coarse horizontal resolutions of $0.5° \times 0.5°$ and $0.2° \times 0.2°$ limits the accurate representation of some convective boundary layer processes, such as daytime convective vertical transport in summer. Future work should therefore incorporate the "skewed turbulence (non-Gaussian / updraft–downdraft) convective boundary layer" scheme and perform a sensitivity anal-

https://doi.org/10.5194/egusphere-2026-2734
Preprint. Discussion started: 11 June 2026

ysis using a shorter LSYNCTIME synchronization interval (e.g. LSYNCTIME $= 300\,s$), which might further enhance model performance at mountain sites.

Code availability. We used atmospheric inverse modeling framework FLEXINVERTv1.0.0 (Thompson and Stohl, 2014) and the source code is provided at https://flexinvert.nilu.no/. For simulations we use FLEXPARTv10.4 (Pisso et al., 2019) and source code is accessible at https://www.flexpart.eu/.

Data availability. Global SF_6 mixing ratios fields are available at https://doi.org/10.25365/phaidra.489 (Vojta et al., 2024).

https://doi.org/10.5194/egusphere-2026-2734
Preprint. Discussion started: 11 June 2026

Table A1. Model configuration in FLEXPARTv10.4.

Configuration	Value	Importance
LDIRECT	-1	Backward mode for computing the SRR
LOUTSTEP	21600 s	Output rate of 6 hr affecting the temporal resolution of output
LOUTAVER	21600 s	Averaged output rate of 6 hr reduces random variability
LOUTSAMPLE	1800 s	Sampling output rate of 30 min is essential for modeling rapid changes
ITSPLIT	999 999 999	Constant particle number
LSYNCTIME	600 s	10 min numerical stability control of synchronizing different physical processes
CTL	-5	Termination of backtrajectory threshold reducing uncertainties in SRR
IFINE	4	Output grid at higher resolution
LSUBGRID	on	Subgrid-scale topography improve flow over steep terrain
LCONVECTION	on	vertical transport by convecting mixing
LAGESPECTRA	on	Transport age diagnostics
CBLFLAG	off	Using Gaussian boundary layer scheme and not a skewed turbulence scheme
Ageclass	604800 s	simulation period of 7 days

https://doi.org/10.5194/egusphere-2026-2734
Preprint. Discussion started: 11 June 2026

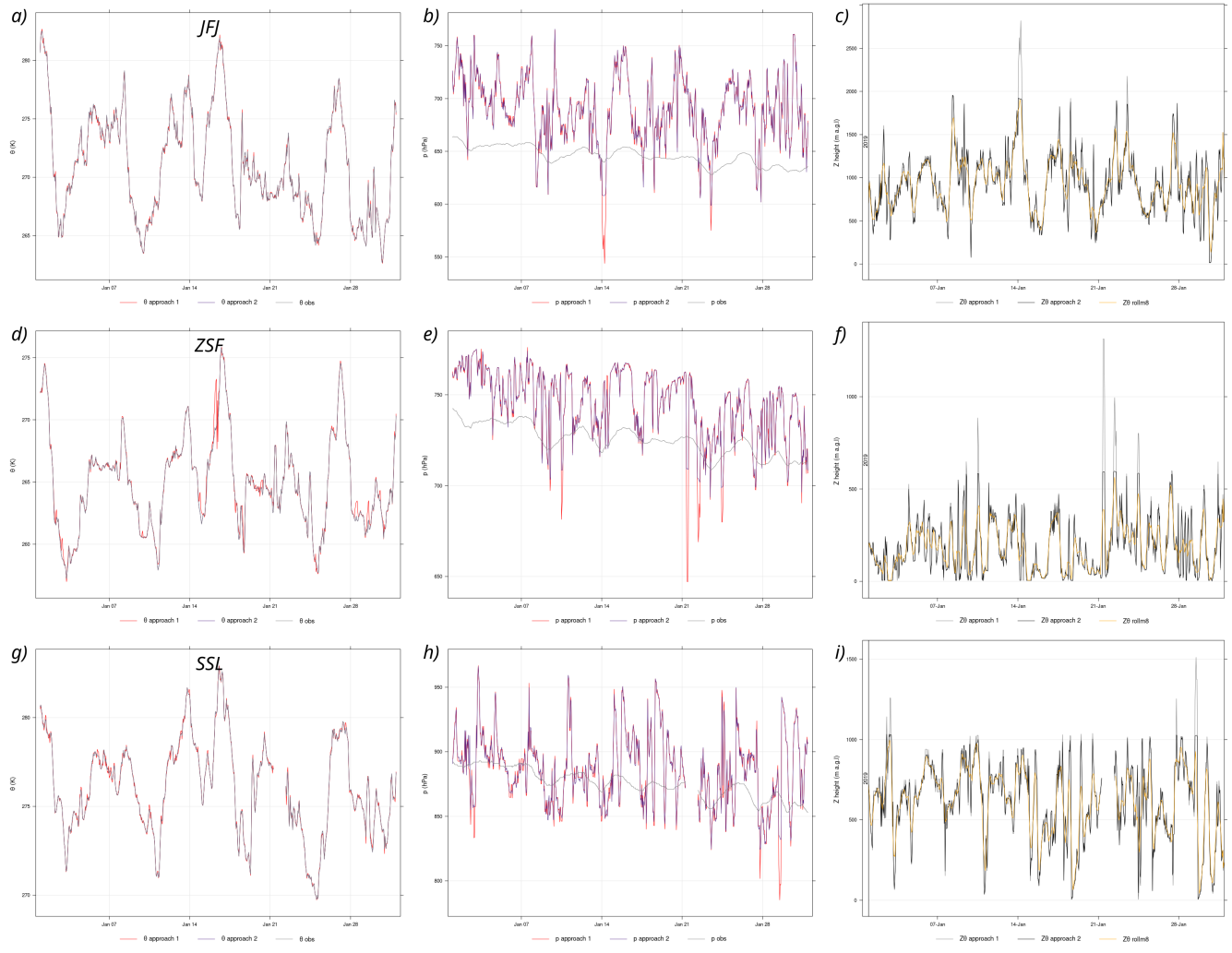

Figure A1. The vertical panels (a,d,g) represents the calculated ERA5 potential temperature with (approach 2) or without (approach 1) pressure limits; panels (b,e,h) are the modeled and observed pressure; and panels (c,f,i) are the calculated model heights for JFJ (top panels), ZSF (middle panels), and SSL (bottom panels) in Jan 2019.

https://doi.org/10.5194/egusphere-2026-2734
Preprint. Discussion started: 11 June 2026

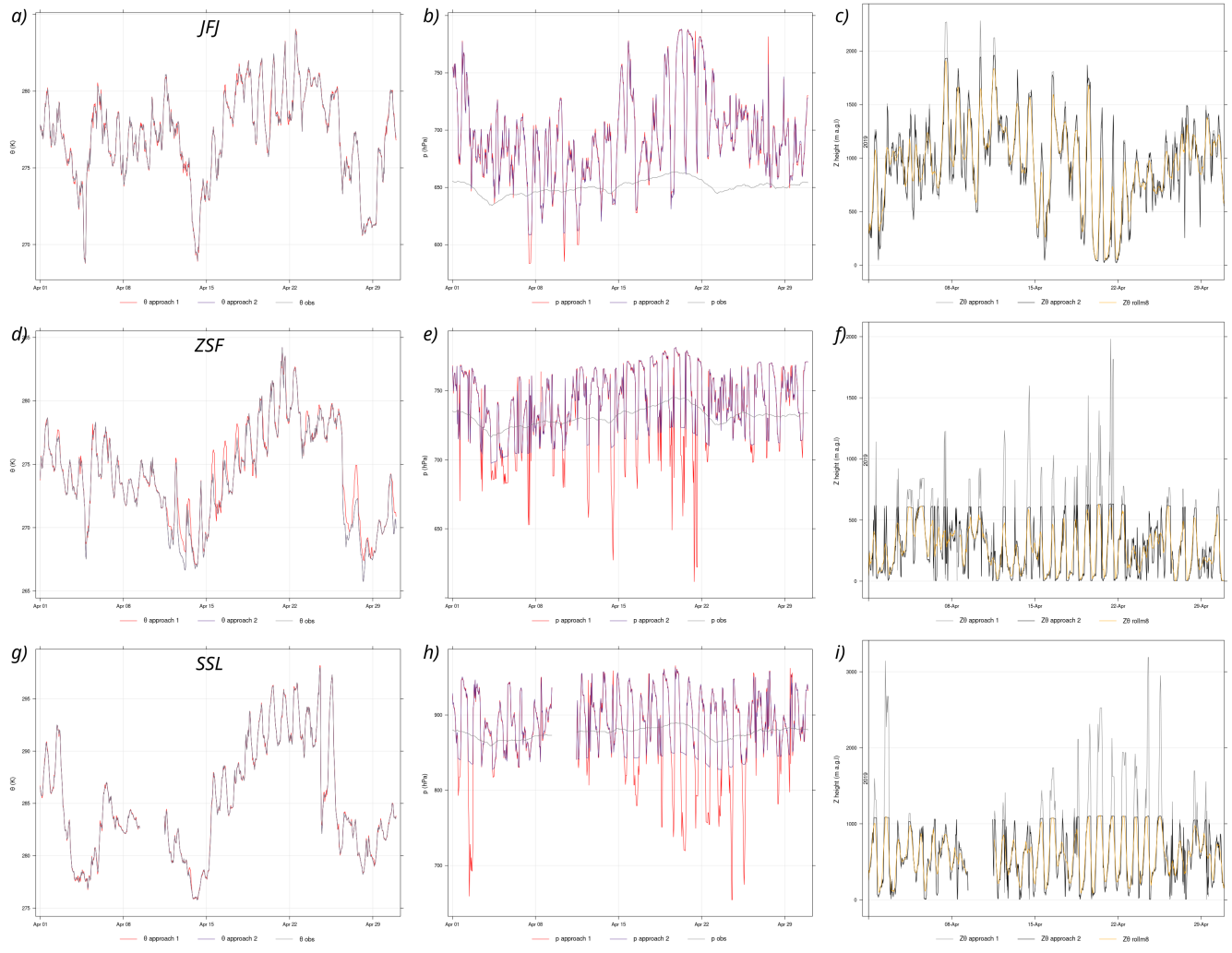

Figure A2. The vertical panels (a,d,g) represents the calculated ERA5 potential temperature with (approach 2) or without (approach 1) pressure limits; panels (b,e,h) are the modeled and observed pressure; and panels (c,f,i) are the calculated model heights for JFJ (top panels), ZSF (middle panels), and SSL (bottom panels) in Apr 2019.

https://doi.org/10.5194/egusphere-2026-2734
Preprint. Discussion started: 11 June 2026

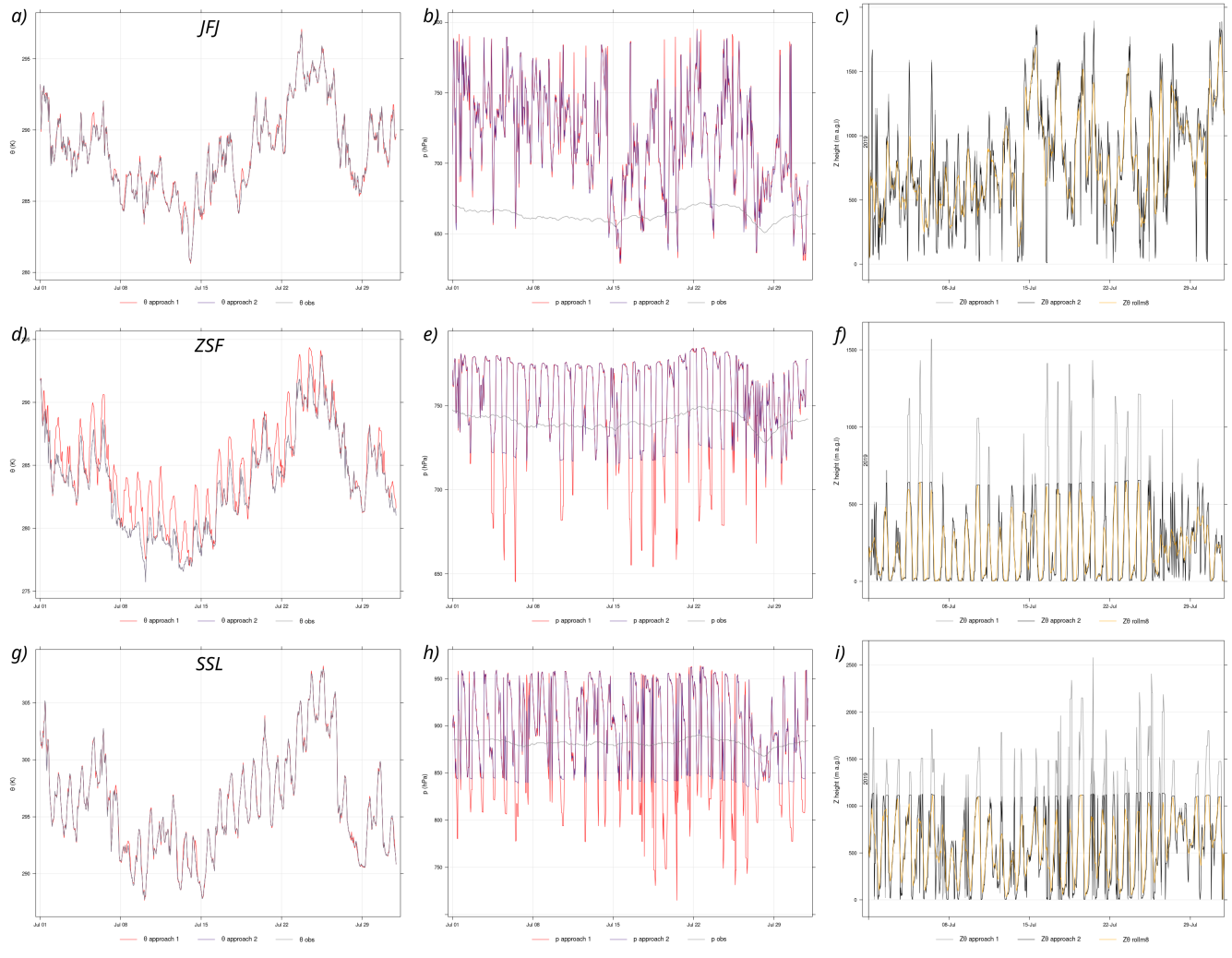

Figure A3. The vertical panels (a,d,g) represents the calculated ERA5 potential temperature with (approach 2) or without (approach 1) pressure limits; panels (b,e,h) are the modeled and observed pressure; and panels (c,f,i) are the calculated model heights for JFJ (top panels), ZSF (middle panels), and SSL (bottom panels) in July 2019.

https://doi.org/10.5194/egusphere-2026-2734
Preprint. Discussion started: 11 June 2026

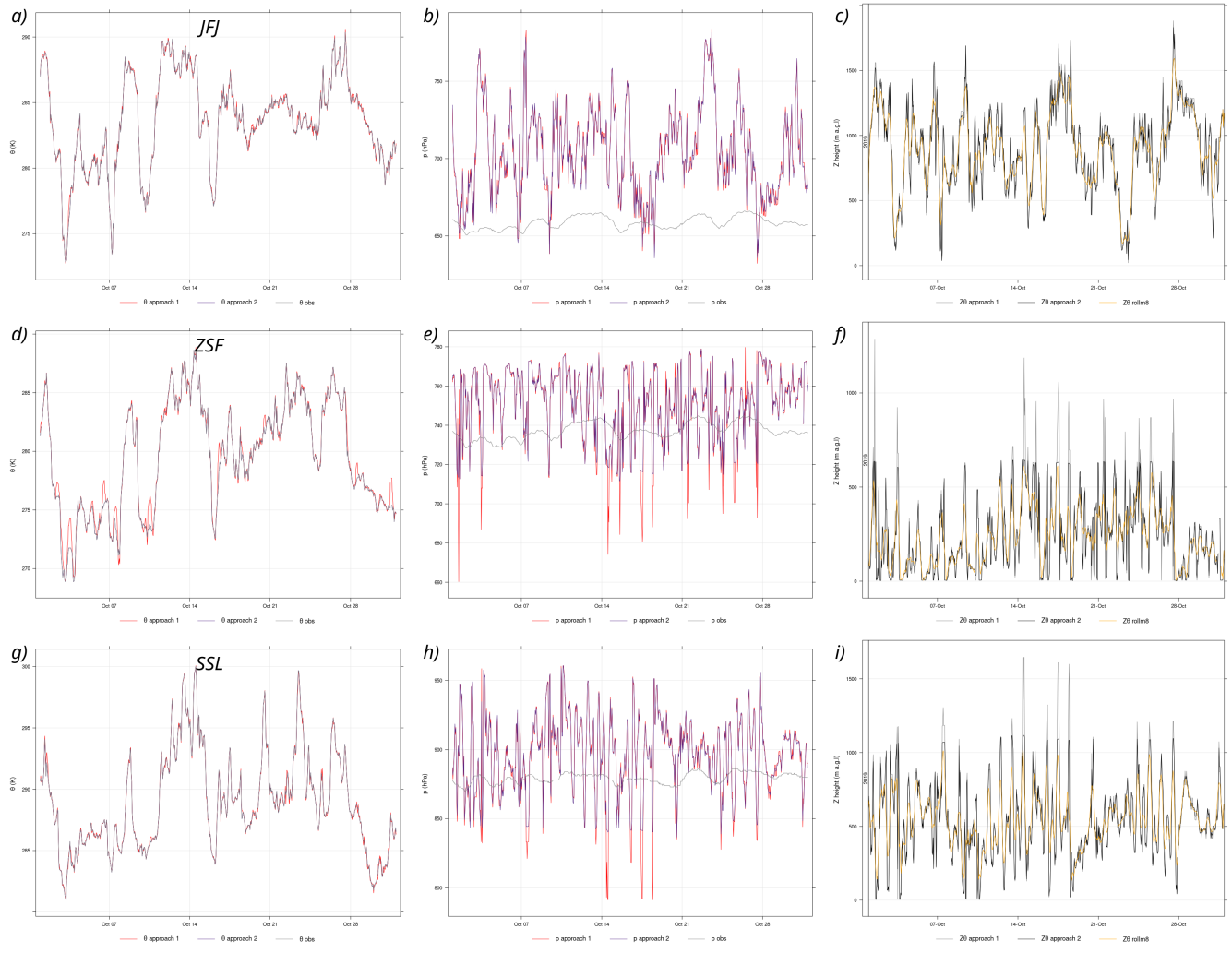

Figure A4. The vertical panels (a,d,g) represents the calculated ERA5 potential temperature with (approach 2) or without (approach 1) pressure limits; panels (b,e,h) are the modeled and observed pressure; and panels (c,f,i) are the calculated model heights for JFJ (top panels), ZSF (middle panels), and SSL (bottom panels) in Oct 2019.

https://doi.org/10.5194/egusphere-2026-2734
Preprint. Discussion started: 11 June 2026

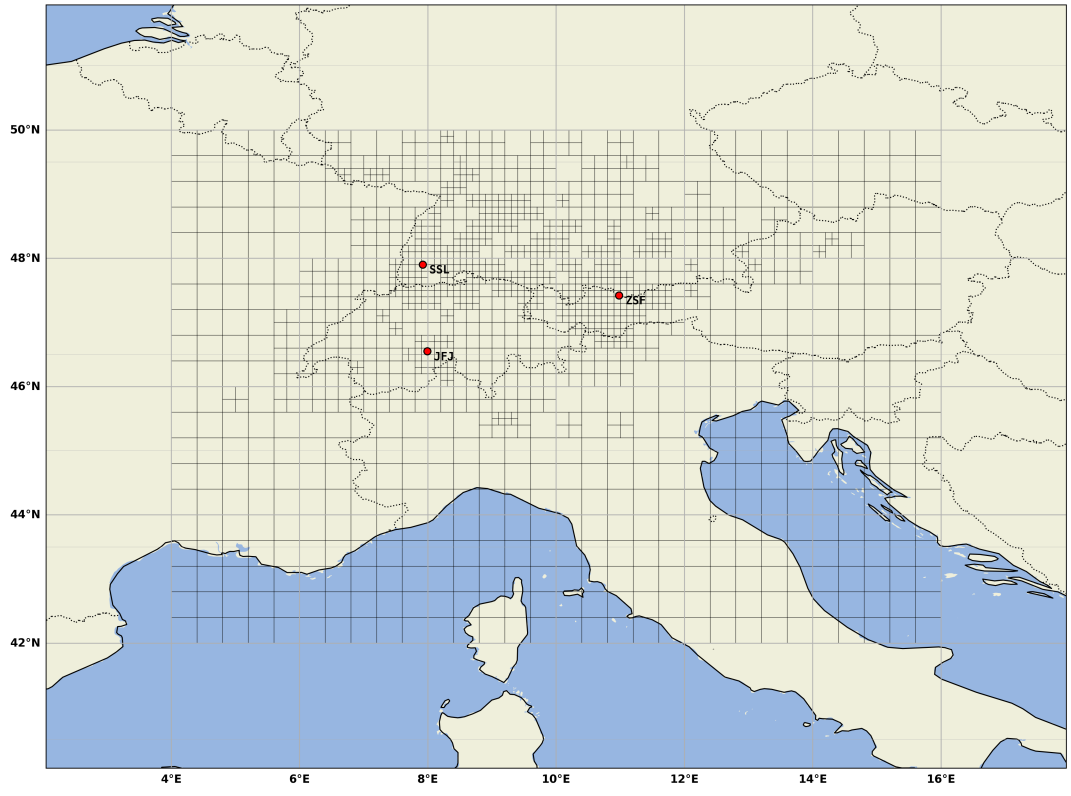

Figure A5. Aggregated grid resolution with finest horizontal resolution of $0.1^\circ \times 0.1^\circ$ based on T-rh source-receptor relationship with $0.5^\circ \times 0.5^\circ$ wind fields, followed by a coarser grid elsewhere.

https://doi.org/10.5194/egusphere-2026-2734
Preprint. Discussion started: 11 June 2026

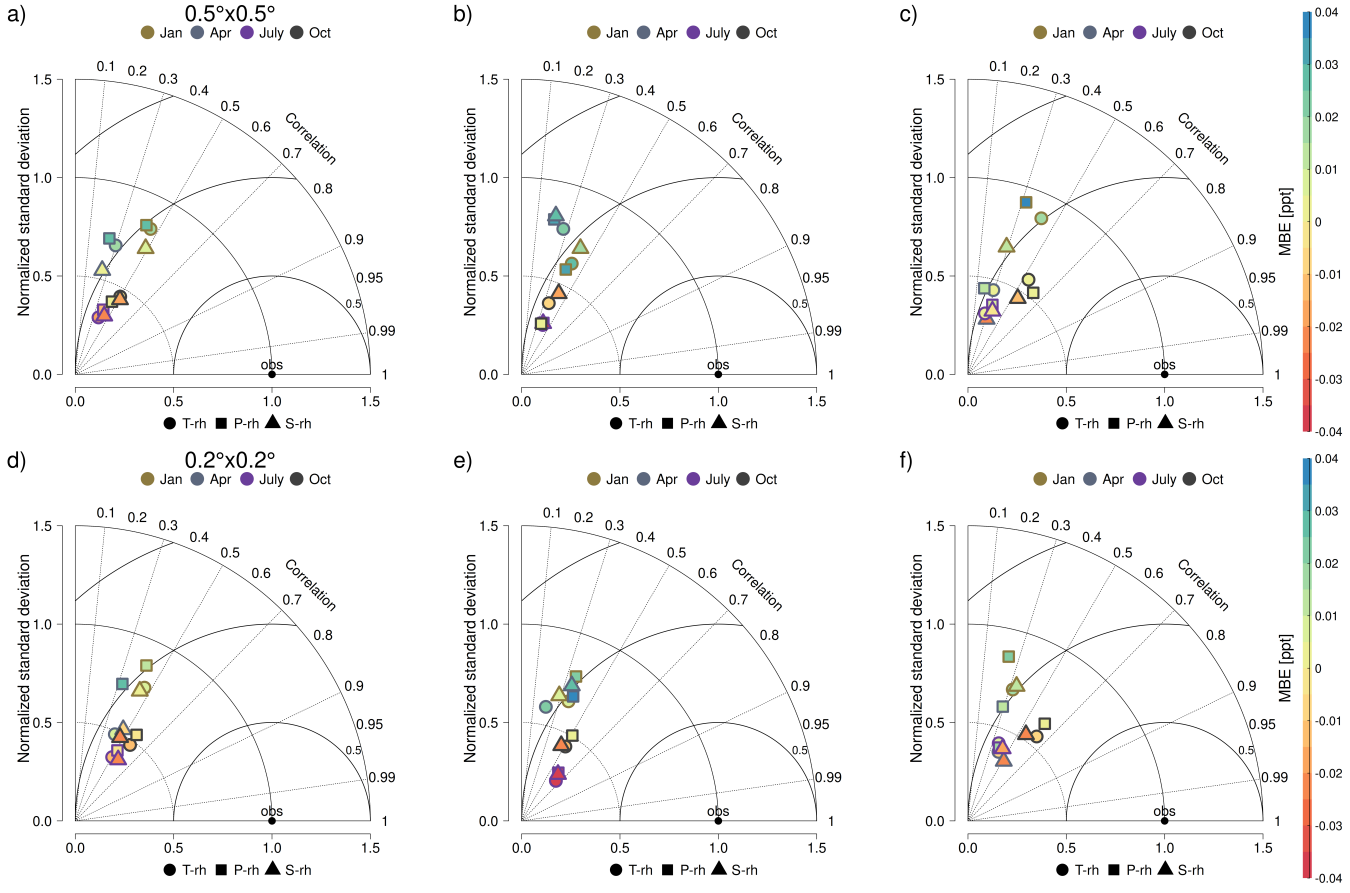

Figure A6. Taylor diagrams for the simulated SF_6 mixing ratios across all release height scenarios and four months at the JFJ station. The error statistics were calculated based on a-d all observations; b-e daytime hours; c-f nighttime hours. Panel a-c was based on ERA5 wind fields at $0.5° \times 0.5°$ spatial resolution, and panel d-f $0.2° \times 0.2°$ resolution.

https://doi.org/10.5194/egusphere-2026-2734
Preprint. Discussion started: 11 June 2026

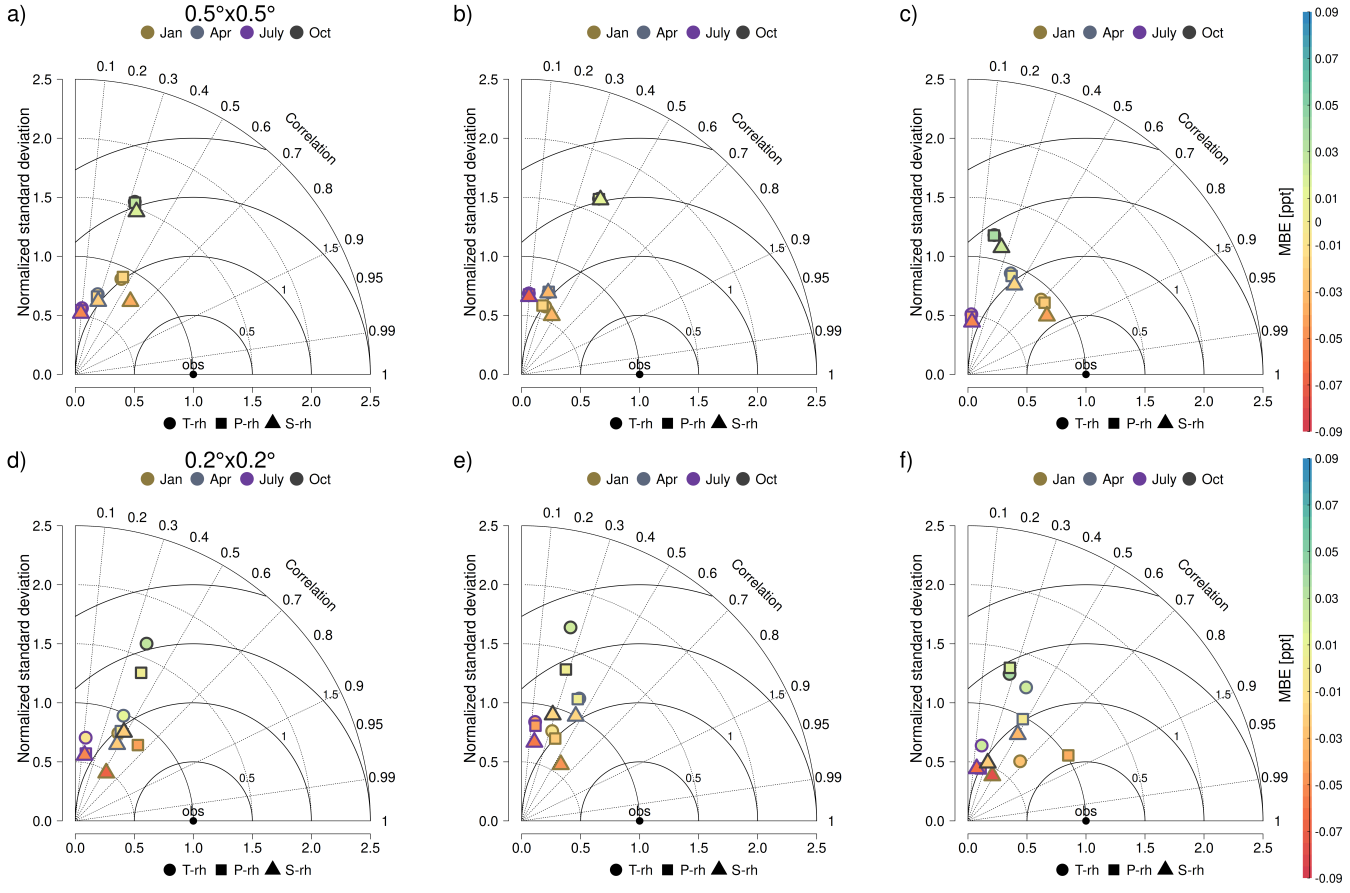

Figure A7. Taylor diagrams for the simulated SF_6 mixing ratios across all release height scenarios and four months at the ZSF station. The error statistics were calculated based on a-d all observations; b-e daytime hours; c-f nighttime hours. Panel a-c was based on ERA5 wind fields at $0.5° \times 0.5°$ spatial resolution, and panel d-f $0.2° \times 0.2°$ resolution.

https://doi.org/10.5194/egusphere-2026-2734
Preprint. Discussion started: 11 June 2026

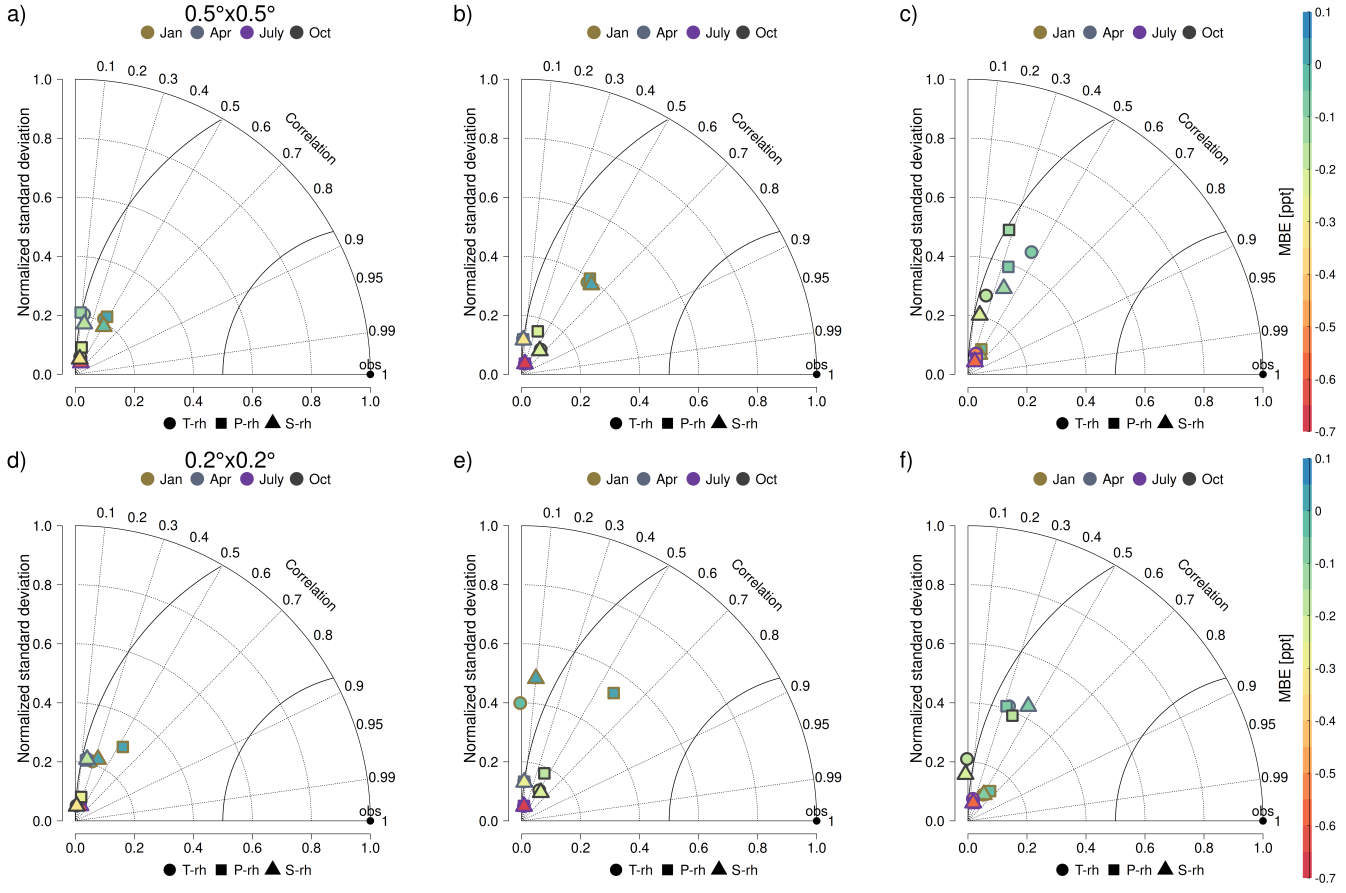

Figure A8. Taylor diagrams for the simulated SF_6 mixing ratios across all release height scenarios and four months at the SSL station. The error statistics were calculated based on a-d all observations; b-e daytime hours; c-f nighttime hours. Panel a-c was based on ERA5 wind fields at $0.5° \times 0.5°$ spatial resolution, and panel d-f $0.2° \times 0.2°$ resolution.

https://doi.org/10.5194/egusphere-2026-2734
Preprint. Discussion started: 11 June 2026

Author contributions. LD is the principal author and has contributed to the technical part (FLEXPART and FlexInvert simulations), analysis, and writing. RLT helped design the study, model setup, and supervision. AB helped design the research and supervision. The final results and content have been evaluated by RLT, AB, IP, and MV.

Competing interests. The contact author declare no competing interests among authors.

Acknowledgements. This paper and related research have been conducted during and with the support of the Italian national inter-university PhD course in Sustainable Development and Climate change (link: www.phd-sdc.it). RLT was supported financially by the European Union's Horizon Europe research and innovation programme under grant agreement No. 101081395.

We acknowledge the World Data Centre for Greenhouse Gases database (WDCGG), Advance Global Atmospheric Gases Experiment (AGAGE), and Integrated Carbon Observation System (ICOS) for providing observational data for JFJ, ZSF, and SSL sites and the following individuals: Martin K. Vollmer, Stefan Reimann, Cedric Couret, and Frank Meinhardt.

https://doi.org/10.5194/egusphere-2026-2734
Preprint. Discussion started: 11 June 2026

References

Bergamaschi, P., Segers, A., Brunner, D., Haussaire, J.-M., Henne, S., Ramonet, M., Arnold, T., Biermann, T., Chen, H., Conil, S., Delmotte, M., Forster, G., Frumau, A., Kubistin, D., Lan, X., Leuenberger, M., Lindauer, M., Lopez, M., Manca, G., Müller-Williams, J., O'Doherty, S., Scheeren, B., Steinbacher, M., Trisolino, P., Vítková, G., and Yver Kwok, C.: High-resolution inverse modelling of European CH_4 emissions using the novel FLEXPART-COSMO TM5 4DVAR inverse modelling system, Atmospheric Chemistry and Physics, 22, 13 243–13 268, https://doi.org/10.5194/acp-22-13243-2022, publisher: Copernicus GmbH, 2022.

Bruch, V., Rösch, T., Jiménez De La Cuesta Otero, D., Ellerhoff, B., Mamtimin, B., Becker, N., Blechschmidt, A.-M., Förstner, J., and Kaiser-Weiss, A. K.: German methane fluxes in 2021 estimated with an ensemble-enhanced scaling inversion based on the ICON–ART model, https://doi.org/10.5194/egusphere-2025-1464, 2025.

Deng, Z., Ciais, P., Tzompa-Sosa, Z. A., Saunois, M., Qiu, C., Tan, C., Sun, T., Ke, P., Cui, Y., Tanaka, K., Lin, X., Thompson, R. L., Tian, H., Yao, Y., Huang, Y., Lauerwald, R., Jain, A. K., Xu, X., Bastos, A., Sitch, S., Palmer, P. I., Lauvaux, T., d'Aspremont, A., Giron, C., Benoit, A., Poulter, B., Chang, J., Petrescu, A. M. R., Davis, S. J., Liu, Z., Grassi, G., Albergel, C., Tubiello, F. N., Perugini, L., Peters, W., and Chevallier, F.: Comparing national greenhouse gas budgets reported in UNFCCC inventories against atmospheric inversions, Earth System Science Data, 14, 1639–1675, https://doi.org/10.5194/essd-14-1639-2022, publisher: Copernicus GmbH, 2022.

Diémoz, H., Barnaba, F., Magri, T., Pession, G., Dionisi, D., Pittavino, S., Tombolato, I. K. F., Campanelli, M., Della Ceca, L. S., Hervo, M., Di Liberto, L., Ferrero, L., and Gobbi, G. P.: Transport of Po Valley aerosol pollution to the northwestern Alps – Part 1: Phenomenology, Atmospheric Chemistry and Physics, 19, 3065–3095, https://doi.org/10.5194/acp-19-3065-2019, publisher: Copernicus GmbH, 2019.

EDGAR, European Commission, Joint Research Centre (JRC), and International Energy Agency (IEA): Emissions Database for Global Atmospheric Research Community GHG Database version 8.0, https://edgar.jrc.ec.europa.eu/dataset_ghg80, 2023.

Folini, D., Ubl, S., and Kaufmann, P.: Lagrangian particle dispersion modeling for the high Alpine site Jungfraujoch, Journal of Geophysical Research: Atmospheres, 113, https://doi.org/10.1029/2007JD009558, _eprint: https://agupubs.onlinelibrary.wiley.com/doi/pdf/10.1029/2007JD009558, 2008.

Forster, P., Storelvmo, T., Armour, K., Collins, W., Dufresne, J.-L., Frame, D., Lunt, D., Mauritsen, T., Palmer, M., Watanabe, M., Wild, M., and Zhang, H.: Chapter 7: The Earth's Energy Budget, Climate Feedbacks and Climate Sensitivity, in: Climate Change 2021 – The Physical Science Basis, edited by Masson-Delmotte, V., Zhai, P., Pirani, A., Connors, S., Péan, C., Berger, S., Caud, N., Chen, Y., Goldfarb, L., Gomis, M., Huang, M., Leitzell, K., Lonnoy, E., Matthews, J., Maycock, T., Waterfield, T., Yelekçi, O., Yu, R., and Zhou, B., pp. 923–1054, Cambridge University Press, 1 edn., ISBN 978-1-009-15789-6, https://doi.org/10.1017/9781009157896.009, 2023.

Giovannini, L., Ferrero, E., Karl, T., Rotach, M. W., Staquet, C., Trini Castelli, S., and Zardi, D.: Atmospheric Pollutant Dispersion over Complex Terrain: Challenges and Needs for Improving Air Quality Measurements and Modeling, Atmosphere, 11, 646, https://doi.org/10.3390/atmos11060646, publisher: Multidisciplinary Digital Publishing Institute, 2020.

Henne, S., Brunner, D., Oney, B., Leuenberger, M., Eugster, W., Bamberger, I., Meinhardt, F., Steinbacher, M., and Emmenegger, L.: Validation of the Swiss methane emission inventory by atmospheric observations and inverse modelling, Atmospheric Chemistry and Physics, 16, 3683–3710, https://doi.org/10.5194/acp-16-3683-2016, publisher: Copernicus GmbH, 2016.

Hersbach, H., Bell, B., Berrisford, P., Hirahara, S., Horányi, A., Muñoz-Sabater, J., Nicolas, J., Peubey, C., Radu, R., Schepers, D., Simmons, A., Soci, C., Abdalla, S., Abellan, X., Balsamo, G., Bechtold, P., Biavati, G., Bidlot, J., Bonavita, M., De Chiara, G., Dahlgren, P., Dee, D., Diamantakis, M., Dragani, R., Flemming, J., Forbes, R., Fuentes, M., Geer, A., Haimberger, L., Healy, S., Hogan, R. J., Hólm, E., Janisková, M., Keeley, S., Laloyaux, P., Lopez, P., Lupu, C., Radnoti, G., de Rosnay, P., Rozum, I., Vamborg, F., Vil-

https://doi.org/10.5194/egusphere-2026-2734
Preprint. Discussion started: 11 June 2026

laume, S., and Thépaut, J.-N.: The ERA5 global reanalysis, Quarterly Journal of the Royal Meteorological Society, 146, 1999–2049, https://doi.org/10.1002/qj.3803, _eprint: https://onlinelibrary.wiley.com/doi/pdf/10.1002/qj.3803, 2020.

Hourdin, F. and Armengaud, A.: The Use of Finite-Volume Methods for Atmospheric Advection of Trace Species. Part I: Test of Various Formulations in a General Circulation Model, Monthly Weather Review, 127, 822–837, https://doi.org/10.1175/1520-0493(1999)127<0822:TUOFVM>2.0.CO;2, 1999.

IPCC, Yamaji, K. M. W., Eggleston, S., Kuramochi, T., Kržan, A., and Properzi, S. O.: Refinement to the 2006 IPCC guidelines for National Greenhouse Gas Inventories, IPCC, Hayama, Japan, https://www.ipcc-nggip.iges.or.jp/public/2019rf/index.html, advance version, 2019.

Lian, J., Lauvaux, T., Utard, H., Bréon, F.-M., Broquet, G., Ramonet, M., Laurent, O., Albarus, I., Chariot, M., Kotthaus, S., Haeffelin, M., Sanchez, O., Perrussel, O., Denier van der Gon, H. A., Dellaert, S. N. C., and Ciais, P.: Can we use atmospheric CO_2 measurements to verify emission trends reported by cities? Lessons from a 6-year atmospheric inversion over Paris, Atmospheric Chemistry and Physics, 23, 8823–8835, https://doi.org/10.5194/acp-23-8823-2023, publisher: Copernicus GmbH, 2023.

Lin, J. C., Gerbig, C., Wofsy, S. C., Andrews, A. E., Daube, B. C., Davis, K. J., and Grainger, C. A.: A near-field tool for simulating the upstream influence of atmospheric observations: The Stochastic Time-Inverted Lagrangian Transport (STILT) model, Journal of Geophysical Research: Atmospheres, 108, https://doi.org/10.1029/2002JD003161, _eprint: https://agupubs.onlinelibrary.wiley.com/doi/pdf/10.1029/2002JD003161, 2003.

Manning, A., O'Doherty, S., Young, D., Redington, A., Say, D., Pitt, J., Arnold, T., Rennick, C., Rigby, M., Wisher, A., Wenger, A., and Simmonds, P.: Long-Term Atmospheric Measurement and Interpretation of Radiatively Active Trace Gases, Tech. Rep. Annual Report, October 2020 – September 2021, UK Government, https://assets.publishing.service.gov.uk/media/62d7b9bee90e071e7e59c97e/verification-uk-greenhouse-gas-emissions-using-atmospheric-observations-annual-report-2021.pdf, 2022.

Meijer, Y., Scholze, M., Pinty, B., Dowell, M., Dolman, H., Heimann, M., Holmlund, K., Denier van der Gon, H., Juvyns, O., Zunker, H., Engelen, R., Janssens-Maenhout, G., Dee, D., Palmer, P., Ciais, P., and Kentarchos, A.: An operational anthropogenic CO emissions monitoring & verification support capacity: needs and high level requirements for in situ measurements : report from the CO monitoring task force, Publications Office of the European Union, ISBN 978-92-76-09004-5, https://data.europa.eu/doi/10.2760/182790, 2019.

Munassar, S., Monteil, G., Scholze, M., Karstens, U., Rödenbeck, C., Koch, F.-T., Totsche, K. U., and Gerbig, C.: Why do inverse models disagree? A case study with two European CO_2 inversions, Atmospheric Chemistry and Physics, 23, 2813–2828, https://doi.org/10.5194/acp-23-2813-2023, publisher: Copernicus GmbH, 2023.

Pisso, I., Sollum, E., Grythe, H., Kristiansen, N. I., Cassiani, M., Eckhardt, S., Arnold, D., Morton, D., Thompson, R. L., Groot Zwaaftink, C. D., Evangeliou, N., Sodemann, H., Haimberger, L., Henne, S., Brunner, D., Burkhart, J. F., Fouilloux, A., Brioude, J., Philipp, A., Seibert, P., and Stohl, A.: The Lagrangian particle dispersion model FLEXPART version 10.4, Geoscientific Model Development, 12, 4955–4997, https://doi.org/10.5194/gmd-12-4955-2019, publisher: Copernicus GmbH, 2019.

Ponomarev, N., Steiner, M., Koene, E., Rubli, P., Grange, S., Constantin, L., Ramonet, M., David, L., Hamzehloo, A., Emmenegger, L., and Brunner, D.: Estimation of CO_2 fluxes in the cities of Zurich and Paris using the ICON-ART CTDAS inverse modelling framework, Atmospheric Chemistry and Physics, 26, 547–570, https://doi.org/10.5194/acp-26-547-2026, 2026.

Ray, E. A., Moore, F. L., Elkins, J. W., Rosenlof, K. H., Laube, J. C., Röckmann, T., Marsh, D. R., and Andrews, A. E.: Quantification of the SF6 lifetime based on mesospheric loss measured in the stratospheric polar vortex, Journal of Geophysical Research: Atmospheres, 122, 4626–4638, https://doi.org/10.1002/2016JD026198, _eprint: https://agupubs.onlinelibrary.wiley.com/doi/pdf/10.1002/2016JD026198, 2017.

https://doi.org/10.5194/egusphere-2026-2734
Preprint. Discussion started: 11 June 2026

Rust, D., Katharopoulos, I., Vollmer, M. K., Henne, S., O'Doherty, S., Say, D., Emmenegger, L., Zenobi, R., and Reimann, S.: Swiss halocarbon emissions for 2019 to 2020 assessed from regional atmospheric observations, Atmospheric Chemistry and Physics, 22, 2447–2466, https://doi.org/10.5194/acp-22-2447-2022, publisher: Copernicus GmbH, 2022.

Seibert, P. and Frank, A.: Source-receptor matrix calculation with a Lagrangian particle dispersion model in backward mode, Atmospheric Chemistry and Physics, 4, 51–63, https://doi.org/10.5194/acp-4-51-2004, publisher: Copernicus GmbH, 2004.

Seinfeld, J. H. and Pandis, S. N.: Atmospheric chemistry and physics: from air pollution to climate change, John Wiley & Sons, 2016.

Simmonds, P. G., Rigby, M., Manning, A. J., Park, S., Stanley, K. M., McCulloch, A., Henne, S., Graziosi, F., Maione, M., Arduini, J., Reimann, S., Vollmer, M. K., Mühle, J., O'Doherty, S., Young, D., Krummel, P. B., Fraser, P. J., Weiss, R. F., Salameh, P. K., Harth, C. M., Park, M.-K., Park, H., Arnold, T., Rennick, C., Steele, L. P., Mitrevski, B., Wang, R. H. J., and Prinn, R. G.: The increasing atmospheric burden of the greenhouse gas sulfur hexafluoride (SF_6), Atmospheric Chemistry and Physics, 20, 7271–7290, https://doi.org/10.5194/acp-20-7271-2020, publisher: Copernicus GmbH, 2020.

Stohl, A., Forster, C., Frank, A., Seibert, P., and Wotawa, G.: Technical note: The Lagrangian particle dispersion model FLEXPART version 6.2, Atmospheric Chemistry and Physics, 5, 2461–2474, https://doi.org/10.5194/acp-5-2461-2005, publisher: Copernicus GmbH, 2005.

Tarantola, A.: 1. The General Discrete Inverse Problem, in: Inverse Problem Theory and Methods for Model Parameter Estimation, Other Titles in Applied Mathematics, pp. 1–40, Society for Industrial and Applied Mathematics, ISBN 978-0-89871-572-9, https://doi.org/10.1137/1.9780898717921.ch1, 2005.

Tarantola, A. and Valette, B.: Inverse Problems = Quest for Information, 50, 159–170, https://www.geophysik.uni-muenchen.de/~igel/Inv-II/Others/Tarantola/IP_QI.pdf, 1982.

Thompson, R., Vojta, M., and Pisso, I.: Implementation and evaluation of the log-normal prior probability distribution in a variational atmospheric inversion framework, Atmos. Chem. Phys. (Atmospheric Chemistry and Physics), submitted, 2025.

Thompson, R. L. and Stohl, A.: FLEXINVERT: an atmospheric Bayesian inversion framework for determining surface fluxes of trace species using an optimized grid, Geoscientific Model Development, 7, 2223–2242, https://doi.org/10.5194/gmd-7-2223-2014, publisher: Copernicus GmbH, 2014.

Thomson, D. J.: Criteria for the selection of stochastic models of particle trajectories in turbulent flows, Journal of Fluid Mechanics, 180, 529–556, https://doi.org/10.1017/S0022112087001940, 1987.

UNFCCC: The Paris Agreement, Tech. rep., United Nations Framework Convention on Climate Change, https://unfccc.int/sites/default/files/english_paris_agreement.pdf, 2015.

Vojta, M., Plach, A., Thompson, R. L., and Stohl, A.: A comprehensive evaluation of the use of Lagrangian particle dispersion models for inverse modeling of greenhouse gas emissions, Geoscientific Model Development, 15, 8295–8323, https://doi.org/10.5194/gmd-15-8295-2022, publisher: Copernicus GmbH, 2022.

Vojta, M., Plach, A., Annadate, S., Park, S., Lee, G., Purohit, P., Lindl, F., Lan, X., Mühle, J., Thompson, R. L., and Stohl, A.: A global re-analysis of regionally resolved emissions and atmospheric mole fractions of SF_6 for the period 2005–2021, Atmospheric Chemistry and Physics, 24, 12 465–12 493, https://doi.org/10.5194/acp-24-12465-2024, publisher: Copernicus GmbH, 2024.

Vojta, M., Plach, A., Thompson, R. L., Purohit, P., Stanley, K., O'Doherty, S., Young, D., Pitt, J., Lan, X., and Stohl, A.: A thousand inversions to determine European SF emissions from 2005 to 2021, EGUsphere, 2025, 1–64, https://doi.org/10.5194/egusphere-2025-1095, 2025.

WMO: Guide to Meteorological Instruments and Methods of Observation, no. 8 in WMO, World Meteorological Organization, Geneva, Switzerland, 7 edn., https://www.weather.gov/media/epz/mesonet/CWOP-WMO8.pdf, 2008.